



Full length article

Separation of K^+ and Bi^{3+} displacements in a Pb-free, monoclinic piezoelectric at the morphotropic phase boundary[☆]

T. Wesley Surta^{a,b}, Lynette Keeney^c, Alicia M. Manjón-Sanz^{d,e}, Catriona Crawford^a, Alexandra Morscher^a, Luke M. Daniels^a, John B. Claridge^{a,b}, Andrew J. Bell^f, Jonathan Alaria^{g,b}, Matthew J. Rosseinsky^{a,b,*}

^a Department of Chemistry, University of Liverpool, Crown Street, Liverpool L69 7ZD, UK

^b Leverhulme Centre for Functional Materials Design, The Materials Innovation Factory, University of Liverpool, 51 Oxford Street, Liverpool L7 3NY, UK

^c Tyndall National Institute, University County Cork, Lee Maltings Complex, Dyke Parade, Cork, Cork T12 R5CP, Ireland

^d CELLS-ALBA Synchrotron, Cerdanyola del Vallès, Barcelona E-08290, Spain

^e Neutron Scattering Division, Oak Ridge National Lab, Oak Ridge, TN 37831, USA

^f Department of Chemical and Process Engineering, University of Leeds, Leeds LS2 9JT, UK

^g Department of Physics, University of Liverpool, Oxford Street, Liverpool L69 7ZE, UK

ARTICLE INFO

Keywords:

Perovskite oxide
Relaxor
Piezoelectric
Ferroelectric
Structural analysis

ABSTRACT

The best piezoelectric properties of any perovskite oxide known are found in the solid solution of the relaxor Pb ($Mg_{1/3}Nb_{2/3}O_3$) and ferroelectric PbTiO₃. Despite its impressive properties, this system has limited analogy. We present the compositional exploration of the Pb-free analogue $(1-x)(K_{1/2}Bi_{1/2})(Mg_{1/3}Nb_{2/3}O_3-x(K_{1/2}Bi_{1/2})TiO_3)$ (KBMN-KBT). We locate the morphotropic phase boundary between $x = 0.86$ and 0.88 changing from Cm to Pm symmetry and the optimally performing composition at $x = 0.88$. We report a piezoelectric figure of merit (d_{33}^*) of 192 pm V^{-1} from strain measurements. Diffraction methods reveal disordered displacements of K^+ and Bi^{3+} which persist from the KBMN endmember through multiple changes in symmetry. Rearrangement of the Bi^{3+} displacements along the uncommon $[011]_c$ direction drives the physical response. Ferroelectric, dielectric, and piezoresponse force microscopy are used to study the progression of physical properties through the MPB and attribute the mechanism to a polarization rotation. Taking account for local, short-range, and average structural features yield a balanced perspective on the structure and properties of this system, isolating the driving force within this system to the Bi^{3+} bonding configuration. This work yields a strong analogy to the Pb-based analogue, and provides strategies for further optimization.

1. Introduction

Piezoelectric materials are key electronic components of many commonplace and developing technologies, such as transducers, actuators, and sensors [1–4]. Of these functional materials, oxides with the ABO_3 perovskite structure exhibit the best performance, with the largest piezoelectric response seen in compounds with Pb^{2+} on the A-site. The industrial standard piezoelectric, $Pb(Zr_{1-x}Ti_x)O_3$ (PZT), is utilized in most applications. The figure of merit typically reported for these materials is the piezoelectric figure of merit (d_{33}), and PZT has a $d_{33} = 200 -$

640 pm V^{-1} [5]. However, environmental, health, and regulatory concerns surrounding the use of toxic Pb^{2+} in electronics have generated great interest in finding Pb-free alternatives.

The search for Pb-free alternatives to PZT has led to many interesting compounds. The mechanism that generates a large piezoelectric response in PZT is a compositionally driven change in symmetry and therefore in the polarization direction. This compositionally driven phase change with a corresponding increase in performance is known as a morphotropic phase boundary (MPB). Zr-rich PZT has a rhombohedral, $R3m$, symmetry, which has a $[111]_c$ polarization vector pointing to

[☆] Compositional exploration of the Pb-free piezoelectric $(1-x)(K_{1/2}Bi_{1/2})(Mg_{1/3}Nb_{2/3}O_3-x(K_{1/2}Bi_{1/2})TiO_3)$ reveals a morphotropic phase boundary and an enhanced piezoelectric response of 192 pm V^{-1} . Structural analysis reveals that the properties are a result of an uncommon $[011]_c$ displacement of Bi^{3+} and the weakening of its bonding interaction with oxygen. A polarization rotation is determined to be entirely responsible for the enhancement in piezoelectric response.

* Corresponding author at: Department of Chemistry, University of Liverpool, Crown Street, Liverpool L69 7ZD, UK.

E-mail address: rossein@liv.ac.uk (M.J. Rosseinsky).

<https://doi.org/10.1016/j.actamat.2023.119594>

Received 9 March 2023; Received in revised form 24 August 2023; Accepted 10 December 2023

Available online 13 December 2023

1359-6454/© 2023 The Authors. Published by Elsevier Ltd on behalf of Acta Materialia Inc. This is an open access article under the CC BY license (<http://creativecommons.org/licenses/by/4.0/>).

the corner of the unit cell, seen in Fig. 1a. The c subscript is used to denote that a vector or lattice plane is relative to the cubic cell. With Ti^{4+} substitution the symmetry of PZT becomes tetragonal, $P4mm$, with a $[001]_c$ polarization vector pointing toward the face of the cell. The MPB lies at the interface ($x \approx 0.52$) of these two symmetries and is believed to have monoclinic Cm symmetry, often referred to as M_A . The displacement vector in this M_A phase lies on the $(110)_c$ plane between the $[111]_c$ and $[001]_c$ vectors, described generally as being in a $[uvw]_c$ direction. The search for and enhancement of Pb-free piezoelectric materials is largely centered around compositionally controlling systems to find an MPB analogous to PZT. The search for M_A -type MPBs has successfully produced many Pb-free piezoelectric systems such as the $(\text{Na}_{1/2}\text{Bi}_{1/2})\text{TiO}_3$ (NBT, $R3c$ $[111]_c$) solid solution with $(\text{K}_{1/2}\text{Bi}_{1/2})\text{TiO}_3$ (KBT, $P4mm$) or BaTiO_3 ($P4mm$).

After decades of searching for PZT analogues, few Pb-free materials have been found which can compete with PZT. This shortcoming indicates that a PZT-based design strategy is perhaps not viable for unlocking large piezoelectric response in Pb-free materials and new strategies should be considered. However, there is a better performing Pb-based piezoelectric system than PZT. The relaxor-based $(1-y)\text{Pb}(\text{Mg}_{1/3}\text{Nb}_{2/3})\text{O}_3$ - $y\text{PbTiO}_3$ (PMN-PT) system has a $d_{33} = 720 \text{ pm V}^{-1}$ in ceramics and has been measured up to 4100 pm V^{-1} in doped single crystals [6,7].

PMN-PT is distinct from PZT in two ways. First, the PMN endmember is a relaxor. Relaxors are a class of materials with cubic, centrosymmetric structures which have local displacements that confer non-centrosymmetric properties [8,9]. The other distinction is the structure around the MPB. PMN is cubic with the polarization believed to be locally $[111]_c$ in character. The symmetry changes to Cm with increasing Ti^{4+} concentration (y) placing the polarization on the $(101)_c$ plane between $[111]_c$ and $[011]_c$ vectors, illustrated in Fig. 1b. In Cm symmetry, when the polarization lies between $[111]_c$ and $[011]_c$ instead of between $[111]_c$ and $[001]_c$ the symmetry is referred to as M_B , distinguishing it from the M_A phase seen in PZT. However, the MPB in PMN-PT is not between Cm and $P4mm$ symmetry as in PZT. At the MPB ($y \gg 0.32$) the symmetry changes from Cm (M_B) to Pm (M_C). The M_C phase places the polarization vector within a $(020)_c$ plane in between $[011]_c$ and $[001]_c$ vectors, illustrated in Fig. 1c. The distinction in the relaxor nature and the different MPB symmetries presents a mechanistic difference, and therefore a piezoelectric design strategy unique from PZT.

We recently reported the first Pb-free material $(\text{K}_{1/2}\text{Bi}_{1/2})(\text{Mg}_{1/3}\text{Nb}_{2/3})\text{O}_3$, KBMN) to have relaxor behavior akin to PMN (a canonical relaxor, i.e., having no ferroelectric ground state) which provides the opportunity to deploy the PMN-PT design concept in a Pb-free system [8, 10]. Indeed, the solid solution was explored through coarse compositional changes in $(1-x)(\text{K}_{1/2}\text{Bi}_{1/2})(\text{Mg}_{1/3}\text{Nb}_{2/3})\text{O}_3$ - $x(\text{K}_{1/2}\text{Bi}_{1/2})\text{TiO}_3$ and showed a peak in the piezoelectric response of $d_{33}^* = 99 \text{ pm V}^{-1}$ at $x =$

0.90 and peak splitting in X-ray diffraction (XRD) data indicative of Pm symmetry. In the present work we enhance the material performance by enhanced control of the composition around $x = 0.90$ to locate the optimally performing composition. Strain as a function of electric field ($S(E)$) is used in conjunction with synchrotron XRD to monitor the compositional enhancement of the d_{33}^* ($S_{\text{max}} / E_{\text{max}}$) and change in symmetry allowing us to locate and characterize an M_B to M_C type MPB. Detailed structural analysis using maximum entropy and Rietveld refinement of the best performing composition ($x = 0.88$) shows how the disordered displacements on the A-site, driven by the electronic configurations of K^+ and Bi^{3+} atoms, persist from KBMN through the MPB and drive the physical response. Importantly, our analysis of the physical response through the MPB shows that the enhanced performance at $x = 0.88$ cannot be attributed entirely to intrinsic or extrinsic factors and therefore must be associated with a polarization rotation between two directions, further supporting the PMN-PT analogy of relaxor-based design for Pb-free piezoelectrics.

2. Results

2.1. Compositional exploration

Compositions in the solid solution were synthesized between $x = 0.70$ and 0.98 to cover the region around $x = 0.90$ that was previously shown to have the best performance [10]. All samples form pure, single-phase perovskites with no indication of impurity phases observed in diffraction patterns, seen in Fig. S1. Samples were made in 20 g batches, to minimize errors in mass when weighing and so powder samples and pellets coming from the same batch were used in powder diffraction and physical property measurements, respectively. The compositions were confirmed by energy-dispersive X-ray spectroscopy and are within error of the nominal composition, Fig. S2.

Our previous report found the piezoelectric properties of $(1-x)\text{KBMN}$ - $x\text{KBT}$ were best at $x = 0.90$ and that this composition had Pm symmetry [10]. The symmetry through the phase diagram changes with composition from cubic ($Pm\bar{3}m$, $x = 0 - 0.60$), to Cm symmetry (M_B , $x \gg 0.60 - 0.85$), then Pm symmetry (M_C , $x \gg 0.85 - 0.95$) to $P4mm$ symmetry when $x > 0.95$. Due to the increased piezoelectric response at $x = 0.90$ and the same Pm symmetry as that seen in the optimally performing PMN-PT composition, we believed the morphotropic phase boundary (MPB) to be in compositional proximity to this compound [11–13].

The composition with the largest piezoelectric response was isolated using the electromechanical strain response. Selected unipolar strain versus electric field ($S(E)$) loops up to 80 kV/cm can be seen in Fig. 2a and data for each sample can be seen in Fig. S3. Ferroelectricity in compositions where $x \geq 0.70$ has been demonstrated, indicating that all of these compositions are noncentrosymmetric [10]. The maximum strain (S_{max}) increases from 0.02% for $x = 0.70$ to a maximum of 0.15%

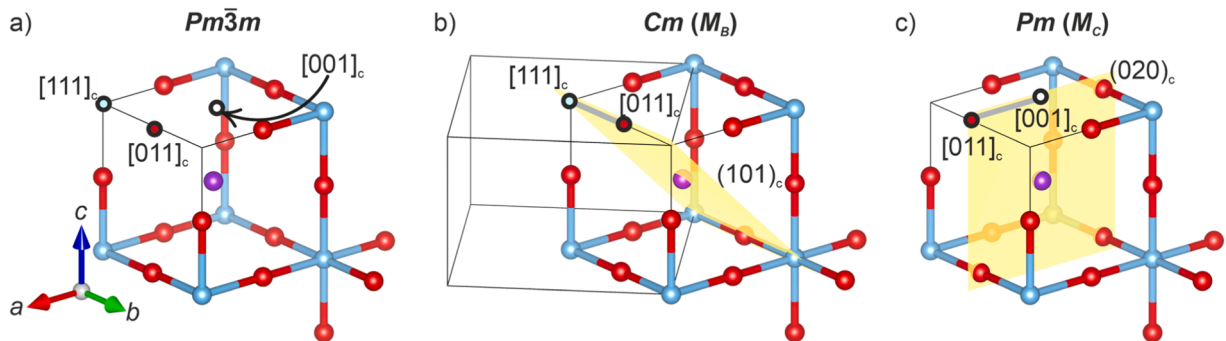


Fig. 1. Schematic diagrams illustrating the polarization allowed in perovskites with (a) showing the $Pm\bar{3}m$ (cubic) perovskite, (b) the Cm (M_B) phase, and (c) the Pm (M_C) phase. In these schematics, A-site (purple), B-site (blue), oxygen (red) atoms and unit cell edges are shown as representing the cubic unit cell. The 45° rotated unit cell of Cm symmetry is also shown in (b). All vectors and lattice planes are labeled with the subscript c as they are relative to the cubic cell.

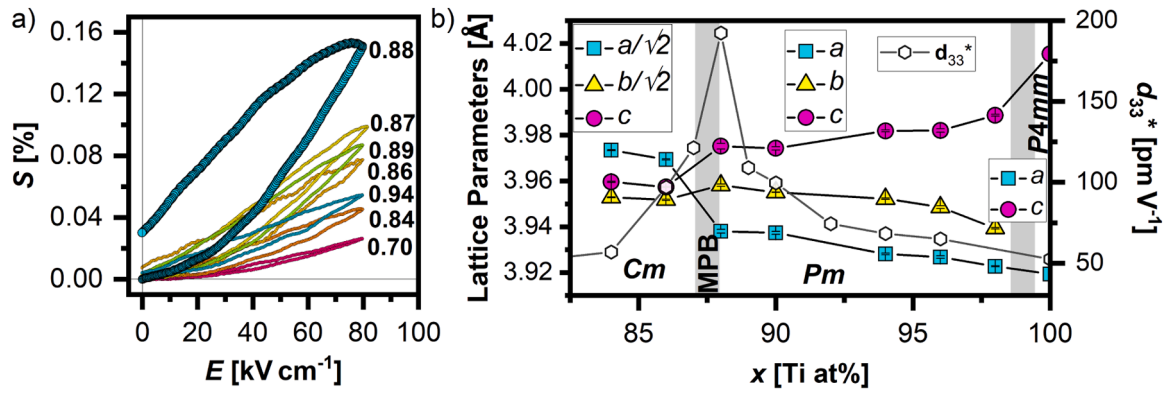


Fig. 2. (a) Strain as a function of electric field ($S(E)$) loops for $x = 0.70, 0.84, 0.86, 0.87, 0.88, 0.89,$ and 0.94 in $(1-x)\text{KBMN}-x\text{KBT}$. (b) Lattice parameters and errors as a function of composition from $x = 0.84, 0.86, 0.88, 0.90, 0.94, 0.96, 0.98,$ and 1.00 . The regions fit with a certain symmetry are labeled with that symmetry and grey regions have been added to separate these regions. All lattice parameters are provided relative to a cubic perovskite for comparison. Lattice parameters for $x = 1.0$ are taken from reference 10. Overlaid with the lattice parameters is the variation in d_{33}^* as a function of composition, further highlighting that the change in symmetry correlates with the increased strain response.

at $x = 0.88$, above which it decreases. These strain values at 80 kV/cm correspond to a $d_{33}^* = 192 \text{ pm/V}$ for $x = 0.88$. This value is almost double the value of 99 pm/V previously reported for $x = 0.90$ [10]. A d_{33}^* of $97, 121,$ and 109 pm/V are observed for $x = 0.86, 0.87,$ and 0.89 , respectively. The large values found in proximity to $x = 0.88$ reveals the narrow compositional window for the MPB in $(1-x)\text{KBMN}-x\text{KBT}$. Values for the measured piezoelectric response are listed in Table S1. Strain was used as a tool to rapidly identify the optimal compositional region. Full characterization of piezoelectric properties by impedance resonance techniques should be perused, however the known difficulty of KBT based ceramics to be sintered and electrically poled make this beyond the scope of this study focused on compositional exploration and structural characterization [14–16]. Ceramic processing, compositional modification, targeted doping strategies to increase resistivity, and identification of the optimal poling will be needed to unlock the full potential of this system.

With the piezoelectric properties identified from the $S(E)$ data, we investigated the structures of these compositions to observe how composition changed the symmetry and better understand the phase diagram. Pawley analysis of synchrotron XRD data was performed on $x = 0.84, 0.86, 0.88, 0.90, 0.92, 0.94,$ and 0.98 to identify the phase boundaries through the solid solution. The results of single-phase fits using the polar subgroups of $Pm\bar{3}m$ are listed in Tables S2–S8. Using these refinements, the symmetries of individual compositions were assigned and the defined phase boundaries are shown in Fig. 2b. For $x = 0.84\text{--}0.86$ Cm (M_B) symmetry fits best, and Pm (M_C) symmetry fits best for $x = 0.88\text{--}0.98$. The lattice parameters and symmetries obtained from compositions can be seen in Fig. 2b. From these fits we can identify two phase boundaries. A boundary is observed between KBT ($P4mm$) and $x = 0.98$ (Pm), illustrating that the symmetry changes with small changes in composition. The other boundary is observed between $x = 0.86$ and 0.88 , changing from Cm and Pm symmetry respectively, and identified as the MPB due to its proximity to $x = 0.88$, which has the largest d_{33}^* . The transition of symmetry from Cm to Pm is the same progression observed in PMN-PT [11,13,17,18]. This change in symmetry is the transition from Cm symmetry with a $[vu\bar{u}]_c$ displacement vector that lies on the $(101)_c$ mirror plane between $[111]_c$ and $[011]_c$ displacements and Pm symmetry with a $[u0v]_c$ displacement vector that lies on the $(020)_c$ mirror plane between $[011]_c$ and $[001]_c$ displacements (Fig. 1b, c).

2.2. Structural analysis

To further understand the structural chemistry that affords the peak piezoelectric response, a Rietveld refinement was carried out to study

the crystal structure of the $x = 0.88$ composition in Pm symmetry. Combined fits to both XRD and neutron powder diffraction (NPD) data were done to provide sufficient contrast to locate local displacements. Initial structural models were generated using lattice parameters from Pawley fits and atomic positions were taken from previous reports on PMN-PT using NPD [13].

The $y = 0.32$ (MPB) composition of $(1-y)\text{PMN}-y\text{PT}$ has Pm symmetry from room temperature to 380 K , above which it adopts $P4mm$ symmetry before becoming cubic at 430 K . Displacements in Pm symmetry lie within the $(020)_c$ mirror plane with the Pb^{2+} displacing 0.140 \AA from the centroid, predominantly (0.132 \AA) along c , and the B-site displacing 0.064 \AA from the centroid entirely along a . This model was modified for use with $(1-x)\text{KBMN}-x\text{KBT}$, $x = 0.88$, by substituting the lattice parameters from the Pawley fit and using the measured composition for $x = 0.88$ (Fig. S2). Atomic positions, atomic displacement parameters, and lattice parameters were allowed to refine yielding a good visual fit to the data.

Using isotropic displacement parameters (B_{iso}) for all atoms yielded an $R_{\text{wp}} = 4.59 \%$, but a large A-site $B_{\text{iso}} = 6.18(5) \text{ \AA}^2$. The use of anisotropic displacement parameters on the A-site made little difference to the fit quality ($R_{\text{wp}} = 4.57 \%$) and yielded an almost spherical displacement tensor, the trace of which yielded an isotropic equivalent of $B_{\text{eq}} = 6.20(16) \text{ \AA}^2$, within error of the simpler model. The oxygen O2 position had a $B_{\text{iso}} = 1.22(6) \text{ \AA}^2$, prompting the use of anisotropic displacement parameters for oxygens. This improved the fit quality ($R_{\text{wp}} = 4.31 \%$) and yielded an A-site $B_{\text{iso}} = 6.26(5) \text{ \AA}^2$. Though this did not reduce the A-site B_{iso} , it did reveal anisotropy within the oxygen sublattice with O1 and O3 being elongated along c and compressed along a and b . This fit using a single A-site position can be seen in Fig. S4, and refined parameters are summarized in Table S9. The large A-site B_{iso} values are not unexpected, and KBMN had a $B_{\text{iso}} = 10.90(18) \text{ \AA}^2$ when fit with a single A-site position [10]. Large B_{iso} values are common in relaxors and have been observed in PMN (3.9 \AA^2), $(\text{K}_{1/2}\text{Bi}_{1/2})(\text{Sc}_{1/2}\text{Nb}_{1/2})\text{O}_3$ (4.6 \AA^2), and PMN-PT ($y = 0.32, B_{\text{iso}} = 2.91(1) \text{ \AA}^2$) [13, 19,20]. Such atomic displacements are attributed to local displacements of the stereochemically active cations that form the basis of polar nanoregions.

Though large A-site atomic displacements parameters are understood to be associated with local displacements, much can be learned from identifying the nature of these displacements [10,19–21]. Fourier difference analysis was first used to identify A-site disorder, seen in Fig. S5. Missing electron density is observed from the XRD data around the A-site and missing nuclear density from the NPD data is distributed in the cell. To fully characterize the local displacements, we employed maximum entropy method (MEM), as it has been shown to be useful in

identifying these displacements [10,22]. Electron density distributions generated from MEM using observed XRD data and the single A-site model can be seen in Fig. S6. These densities show that there is significant A-site disorder. Contour maps of the (002)_c plane show that the observed electron density (Fig. S6a) is elongated along *a* with two maxima that are not accounted for by the single A-site position in the calculated model (Fig. S6b).

To account for this, the atomic positions of K⁺ and Bi³⁺ were unconstrained, allowing independent refinement with separate coordinates. The refined position for the single A-site model was used for Bi³⁺ and K⁺ was placed at the center of the unit cell, reflecting the disorder observed in the Fourier difference and MEM maps and consistent with the A-site chemistry seen in KBMN [10]. All parameters were refined, the fit quality improved ($R_{wp} = 4.20\%$), and the visual fit to the data was still good. While the persistence of the good visual fit (Fig. S7) and improvement of fit quality parameters (Table S10) is positive, the A-site B_{iso} values render the model questionable. The B_{iso} value for K⁺ is reduced to a reasonable value of $1.13(5) \text{ \AA}^2$, but the B_{iso} for Bi³⁺ increases to $6.85(11) \text{ \AA}^2$ (Table S10). The atomic positions of these two A-sites have separated significantly. The K⁺ is displaced almost entirely along the *c*-axis, with the *z* position refining to $0.595(3)$ and the *x* position refining to $0.503(6)$, which is within error of the centroid along *a*. The Bi³⁺ is refined from its initial position of $(0.5343(13), 0.5, 0.5355(11))$ to $(0.539(2), 0.5, 0.5191(16))$, which represents a new displacement which is predominantly along the *a*-axis. The large B_{iso} value ($6.85(11) \text{ \AA}^2$) for Bi³⁺ in this displaced refinement indicates that the model can be improved further and capture more information about the local A-site displacements.

Local displacements were once again investigated using MEM (Fig. S8), but this time using the model where K⁺ and Bi³⁺ have separate atomic positions. Despite K⁺ and Bi³⁺ having different positions, the calculated electron density is similar to the single A-site structural model (Fig. S6), but the center of the electron density is different. Contour plots of the (020)_c plane (Fig. S8c, d) show that this off-centering seen in the calculated electron density is closer to that of the observed. The observed electron density for the two A-sites (Fig. S8a and c) model is very close to the single A-site model (Fig. S6 a and c). The contour plot of observed electron density along the (002) plane (Fig. S9a) shows a peak in intensity in the center that is rectangular and has features protruding out from it along the *b*-axis, on either side of the (020)_c mirror plane.

To capture this shape in the electron density, the Bi³⁺ was separated into two sites. One site remained on the (020)_c mirror plane (1*b* position) and one site was displaced off the mirror plane (2*c* position). The occupancies of these Bi³⁺ sites were set to contain 50 % of the Bi³⁺ and refined while maintaining the overall Bi³⁺ content of the material. All parameters were refined, including the Bi³⁺ occupancy, yielding a stable refinement and an improvement in fit quality ($R_{wp} = 4.11\%$). Furthermore, the A-site B_{iso} values decreased for K⁺ (1*b* position) to $0.34(11) \text{ \AA}^2$ and to $1.9(3)$ and $2.18(18) \text{ \AA}^2$ for Bi³⁺ on the 1*b* and 2*c* sites, respectively. These values are consistent with what is expected for a cation on the A-site of a perovskite oxide.

A fit using *Cm* symmetry was attempted for this composition as well. All attempts to fit the data resulted in high fit quality parameters ($R_{wp} \geq 4.54\%$), large atomic displacement values ($B_{iso} > 2.89(16) \text{ \AA}^2$), and a poor visual fit to the data, being unable to fit key reflections (e.g. (002)_c), see Fig. S10 and Table S11. The inability to fit the data to *Cm* symmetry removes any ambiguity of the symmetry at the MPB. The final model for $x = 0.88$ has *Pm* symmetry, one K⁺ site, and two Bi³⁺ sites and was arrived at from the combination of a good visual fit to the data, a best fit quality parameter for any model attempted, and chemically reasonable refined parameters. This model is further supported by MEM analysis. Fig. 3a–d shows the observed and calculated electron density distributions, and their contour plots match well, confirming that our model reproduces the observed data well. The fit of this model can be seen in Fig. 3e, f and the refined parameters are listed in Table 1.

2.3. Structural description

The resultant structure is shown in Fig. 4a. The structural parameters seen in Table 1 show that this monoclinic perovskite has a smaller unit cell than KBMN ($4.046490(4) \text{ \AA}$), PMN ($4.0500(2) \text{ \AA}$), or PMN-PT ($y = 0.32, 4.0046(2) - 4.0281(3) \text{ \AA}$) [10,13,19]. Furthermore, $x = 0.88$ has a smaller *b* angle of $90.1131(12)^\circ$, compared to $90.178(5)^\circ$ for PMN-PT ($y = 0.32$).

The three A-site polyhedral environments seen in Fig. 4b–d are distinctly different from each other, but reminiscent of the KBMN end-member. The K⁺ environment, Fig. 4b, does not have as large of a displacement off the centroid as the Bi³⁺ positions. There is a $0.186(9) \text{ \AA}$ displacement of K⁺ from the centroid, which is almost entirely (0.183 \AA) along the *c*-axis, or $[001]_c$ in character. This displacement is smaller than the $0.441(7) \text{ \AA}$ and $0.640(16) \text{ \AA}$ displacements of the Bi³⁺ or the $0.5901(11)$ and $0.6005(17) \text{ \AA}$ displacements for Bi³⁺ in KBMN [10]. However, this K⁺ displacement is notably larger than the 0.140 \AA displacement for Pb²⁺ in PMN-PT $y = 0.32$. The shortest and longest K-oxygen bonds are between K⁺ and the O3 oxygens, $2.567(10)$ and $3.060(11) \text{ \AA}$, respectively. The O3 position is notably anisotropic along *c* highlighting the disorder associated with this environment. Other K-oxygen bond lengths are $2.707(19) - 2.881(19) \text{ \AA}$, which are consistent with those seen in other perovskites, e.g. KNbO₃, $2.75 - 2.89 \text{ \AA}$ [23].

The Bi³⁺ is found in two different environments. The Bi³⁺ that lies on the 1*b* position, on the (020)_c mirror plane, has a displacement towards the face of the cell almost entirely in the $[100]_c$ direction, Fig. 4c. Since the displacement is predominantly $[100]_c$ in character, this environment will be referred to as the Bi $[100]$ site. This environment generates four short Bi-O bonds with two equal Bi-O2 bonds of $2.361(13) \text{ \AA}$ and two different Bi-O1 bonds that are $2.35(3)$ and $2.44(3) \text{ \AA}$. These bond lengths reasonably compare with other short Bi-O bonds seen in perovskite oxides, such as BiFeO₃ (2.365 \AA) [24]. The KBMN relaxor end-member has a similar bonding environment for Bi³⁺ where it is displaced towards the face of the cell. In KBMN there are four short bonds which are equal and slightly longer at $2.473(4) \text{ \AA}$. The Bi $[100]$ in $x = 0.88$ displaces $0.640(16) \text{ \AA}$ from the centroid, with 0.639 \AA along the *a*-axis and 0.028 \AA along the *c*-axis. This is again in contrast to the equivalent environment in KBMN where the Bi³⁺ displaces only $0.6005(17) \text{ \AA}$ from the centroid.

The other Bi³⁺ site lies on a 2*c* general position, and therefore is off the (020)_c mirror plane, seen in Fig. 4d. This Bi³⁺ is displaced towards the corner of the cell and generates three short bond distances of $2.489(12)$, $2.499(18)$, and $2.530(15) \text{ \AA}$ for Bi-O1, O2, and O3, respectively. Once again, KBMN has a similar Bi³⁺ environment with three short bonds of $2.404(4) \text{ \AA}$. The bonding environment generated in both these compounds is analogous to a rhombohedral ($R3c, [111]_c$) environment that is what is seen in the few ambient pressure accessible, all Bi³⁺ A-site perovskites, such as BiFeO₃ and $\text{Bi}(\text{Ti}_{3/8}\text{Fe}_{2/8}\text{Mg}_{3/8})\text{O}_3$ [24,25]. However, despite the three short bonds in $x = 0.88$ this Bi³⁺ displacement is primarily $[01\bar{1}]_c / [0\bar{1}1]_c$ in nature relative to the centroid. Due to this displacement character, this site will be referred to as Bi $[011]$. Looking at the other Bi-O bonds around this environment, there is one medium length bond ($2.597(18) \text{ \AA}$), and the remaining eight Bi-O bond lengths are between $2.708(16)$ and $3.151(17) \text{ \AA}$. The displacement off the centroid is $0.441(7) \text{ \AA}$ with 0.300 and 0.313 \AA along the *b* and *c*-axes respectively, but only 0.076 \AA along the *a*-axis. The equivalent position in KBMN has a shorter displacement of $0.5901(11) \text{ \AA}$. Disordered displacements of Bi³⁺ have been seen along $[111]_c$ and $[001]_c$ directions have been seen KBMN, KBT, $(\text{Na}_{1/2}\text{Bi}_{1/2})\text{TiO}_3$, and $\text{BiFeO}_3\text{-BaTiO}_3$ before, but the $[011]_c$ is unique in a Bi³⁺ based system [10,26–31].

The occupancies of the two Bi³⁺ sites were constrained together to equal the stoichiometry but refined between the sites. The refined occupancy of the Bi $[100]$ site is $0.127(11)$ which corresponds to 25.6 % of the Bi³⁺ in the structure, with the other 74.4 % on the Bi $[011]$ site. Though the Bi $[100]$ and Bi $[011]$ sites have equivalent positions in

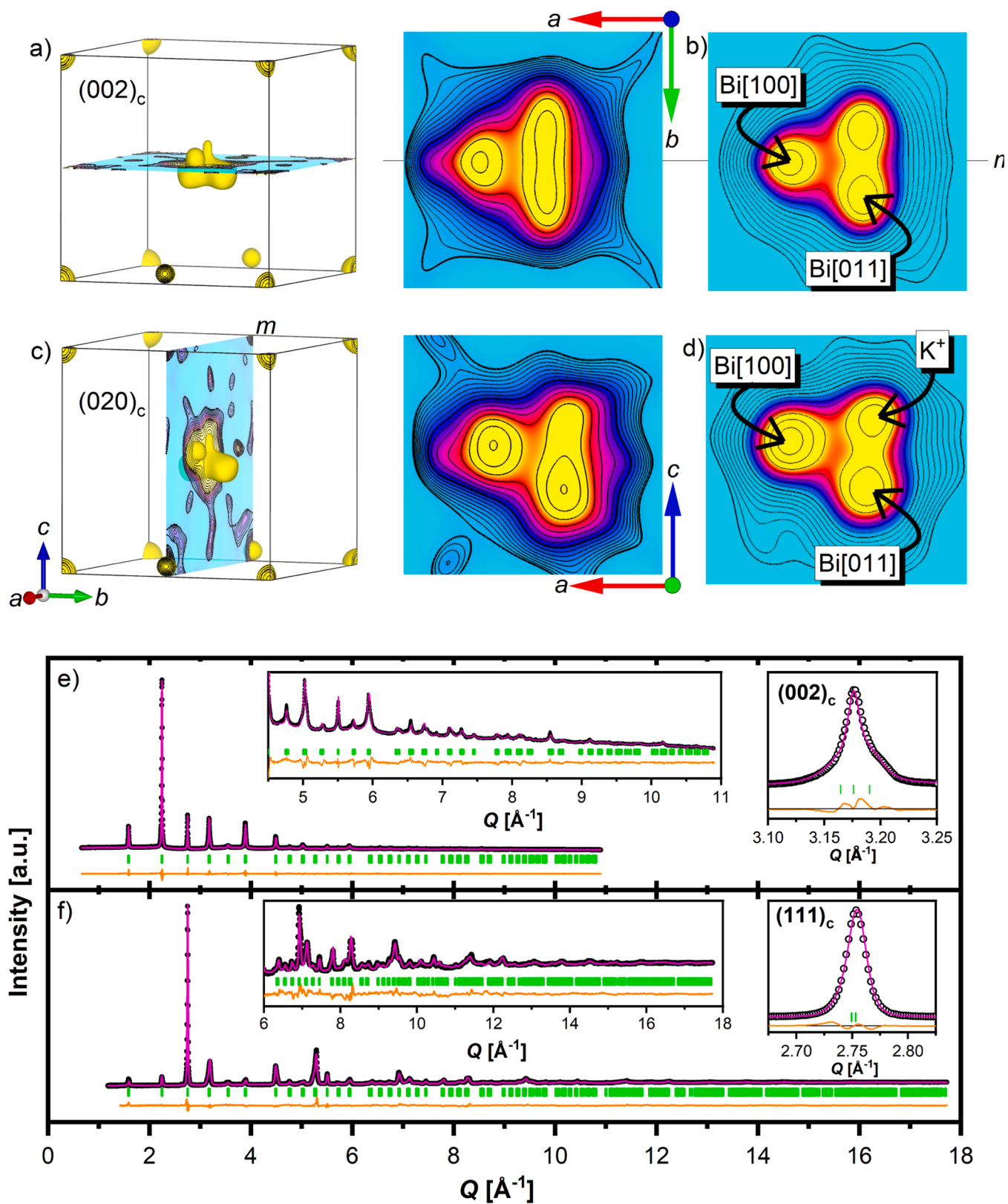


Fig. 3. Structural details for $x = 0.88$ in $(1-x)\text{KBMN}-x\text{KBT}$ using the final model in Pm symmetry, with one K^+ position and two Bi^{3+} positions. Contour plots of the electron density generated using MEM showing the $(002)_c$ plane can be seen for the (a) observed and (b) calculated structure factors. Contour plots showing the $(020)_c$ plane can be seen for the (c) observed and (d) calculated structure factors. The $(020)_c$ mirror plane has been labeled with an m and the calculated electron density contour plots (b) and (d) have had the A-site atom positions labeled. Final Rietveld fits of (e) XRD and (f) NPD data. Insets of the high Q regions are shown for both data sets, and a fit to the profile of the $(002)_c$ peak is shown for the XRD and the $(111)_c$ peak for the NPD data. Observed data are shown as black circles, the calculated diffraction pattern is a magenta line, the difference is an orange line, and hkl tick marks are shown in green.

Table 1

Refined parameters for final Rietveld refinement in Pm symmetry with one K^+ position and two Bi^{3+} positions. Atomic displacement parameters for the oxygens were fit anisotropically and the trace of the displacement is shown in square brackets.

$R_{wp} = 4.11\%$			$R_p = 3.11\%$			G.O.F = 3.35			
Atom	Site	Wyckoff Position	x	y	z	Occ	A-site%	$B_{iso}(\text{\AA}^2)$	
K^+	K	1b	0.503(4)	0.5	0.570(2)	0.5	50	0.34(11)	
Bi^{3+}	Bi [100]	1b	0.657(4)	0.5	0.531(4)	0.127(11)	12.7(11)	1.9(3)	
Bi^{3+}	Bi [011]	2c	0.514(2)	0.5758(13)	0.445(2)	0.1865	37.3	2.18(18)	
Mg^{2+}	B-site	1a	0	0	0	0.04		0.72(4)	
Nb^{5+}	B-site	1a	0	0	0	0.08		0.72(4)	
Ti^{4+}	B-site	1a	0	0	0	0.88		0.72(4)	
O^{2-}	O1	1b	0.997(4)	0.5	0.045(3)	1		[0.795]	
O^{2-}	O2	1a	0.984(3)	0	0.545(2)	1		[1.101]	
O^{2-}	O3	1a	0.508(3)	0	0.983(2)	1		[3.055]	
$a = 3.93883(18)\text{\AA}$			$b = 3.95639(14)\text{\AA}$			$c = 3.9707(3)\text{\AA}$			
$\alpha = 90.1131(12)^\circ$									
Site	$U_{11}(\text{\AA}^2)$	$U_{22}(\text{\AA}^2)$	$U_{33}(\text{\AA}^2)$	$U_{13}(\text{\AA}^2)$					
O1	0.011(3)	0.0022(19)	0.016(5)	0.000(8)					
O2	0.019(4)	0.010(3)	0.012(5)	0.000(5)					
O3	0.0035(15)	0.007(3)	0.105(8)	-0.018(4)					

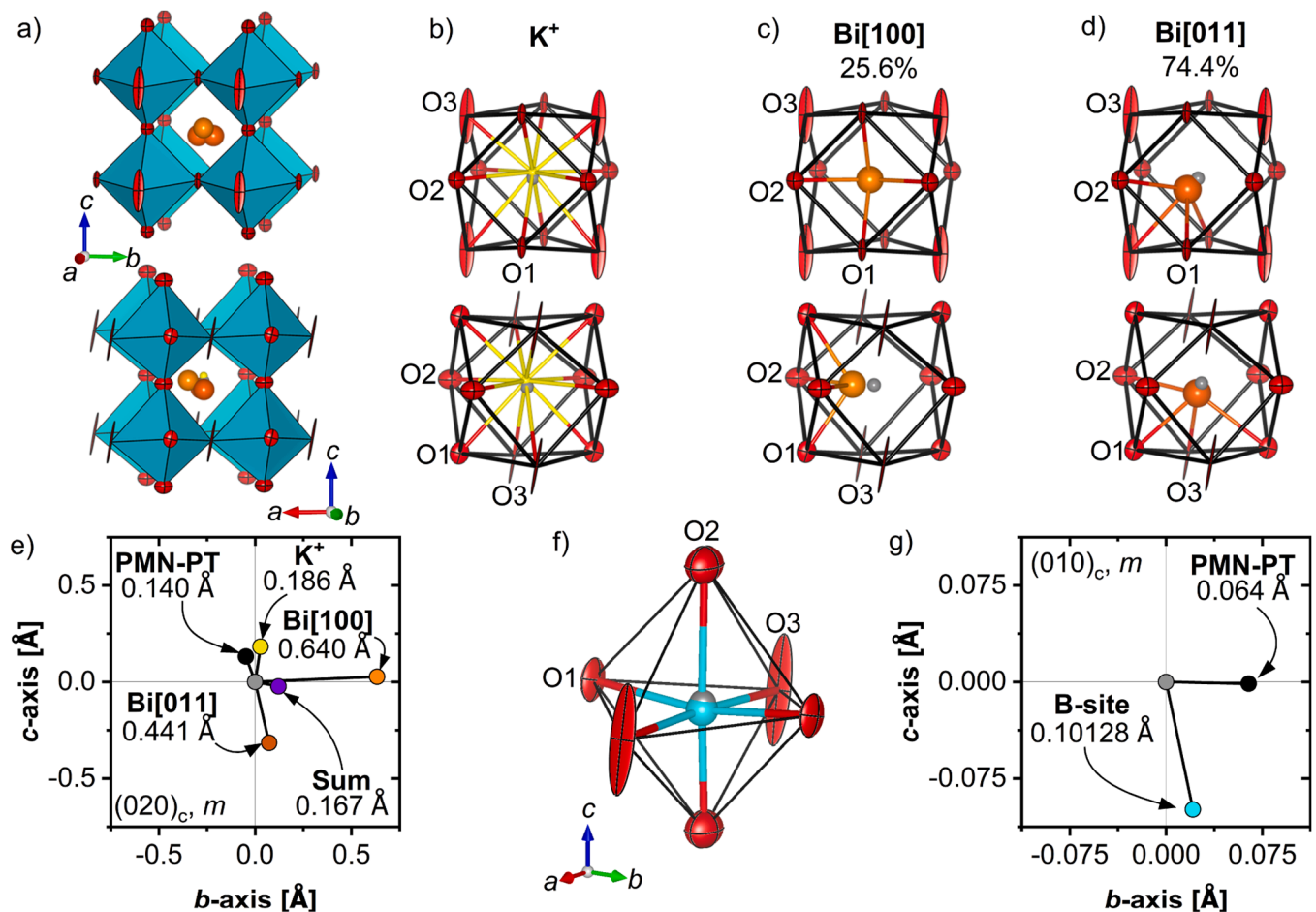


Fig. 4. (a) Final refined structure for the $x = 0.88$ of the $(1-x)KBMN-xKBT$ solid solution in Pm symmetry viewed along a and b-axes. A-site polyhedral environments for the (b) K^+ (yellow), (c) $Bi[100]$ (orange), and (d) $Bi[011]$ (burnt orange) sites. The polyhedral centroid is shown in grey in each of these environments. (e) A summary of the A-site displacement vectors found in $x = 0.88$ within the $(020)_c$ mirror plane. The centroid is grey, the K^+ is yellow, the $Bi[100]$ is orange, the $Bi[011]$ is burnt orange, their vector sum is purple, and the displacement found for Pb^{2+} in $y = 0.32$ in $(1-y)PMN-yPT$ is black. Polarization is limited to the $(020)_c$ and $(010)_c$ mirror planes in Pm symmetry. (f) B-site (cyan) polyhedral environment, with the polyhedral centroid shown in grey. (g) Summary of the B-site displacement vectors for KBMN-KBT (cyan) and PMN-PT (black) at the MPB, displayed within the $(010)_c$ mirror plane.

KBMN, the difference in occupancy shows a key distinction. In KBMN, most of the of the Bi^{3+} (64 %) is on the $Bi[100]$ equivalent site with the remaining 36 % on the other site. As the Ti^{4+} concentration is increased from $x = 0$ to 0.88, the population of the $Bi[100]$ decreases. Additionally, bond lengths for this $Bi[100]$ site decreases while its displacement

increases. Conversely, the $Bi[011]$ occupancy increases, the bond lengths increase, and the displacement decreases, resulting in a Bi^{3+} atom which is less tightly bound to a set of oxygens and therefore more susceptible to displacement by an electric field. The increase in occupancy of Bi^{3+} on the $Bi[011]$ site is consistent with Bi^{3+} seeking a

rhombohedral bonding environment typical for an ambient pressure perovskite oxide [10,22,25,32,33]. The reason for the high occupancy of this positions is unclear, but should be studied further with microscopy, spectroscopy, or theory to isolate the local or short range driving force of this site partitioning.

This increase in occupancy to seek a preferred bonding configuration in combination with the weakening (i.e. lengthening) of the Bi-O bonds is likely the chemical origin of this MPB. Furthermore, the Bi³⁺ seeking this rhombohedral-like bonding configuration yet yielding an uncommon [011]_c type displacement while between two phases, KBMN and KBT, which prefer Bi³⁺ to displace in a [001]_c direction is unique. This bonding and displacement configuration indicates how the electronic structure of Bi³⁺ is driving the physical response in this system, yielding insights into further tuning this system and the design of Bi-based relaxor MPBs. A summary of the A-site displacement configurations and their vector sums within the (020)_c mirror plane can be seen in Fig. 4e. This figure shows that the large [00 $\bar{1}$]_c displacement of the Bi [011] site cancels the [001]_c displacement character of the K⁺ and Bi [100] sites resulting in a net [100]_c displacement vector for the A-sites in $x = 0.88$.

The refined B-site environment can be seen in Fig. 4f. This site is less disordered and has a smaller B_{iso} (0.72(4) Å²) than the A-sites, which refined stably for each model explored. Bond lengths are between 1.804 and 2.169 Å and there is a total displacement from the centroid of 0.10128(10) Å. The displacement is primarily in the [00 $\bar{1}$]_c direction, with a displacement of 0.09906 Å along the *c*-axis and 0.02090 Å along the *a*-axis. The large displacement along [00 $\bar{1}$]_c for the B-site correlates with the Bi[011] displacements, generating a larger net dipole in this direction. A combination of the anti-polar K⁺ and Bi[100] displacements along the *c*-axis and the large displacement of the Bi[100] along the *a*-axis would prevent the correlation of all displacements along the *c*-axis, suppressing the *P4mm* symmetry seen in pure KBT ($x = 1$). Of note is the large anisotropy of the O3 thermal ellipsoid with significant elongation of this atom along the *c*-axis and compression along *a*. There is strong interaction between this site and both the B-site (1.939(12) Å) and Bi [011] site (2.489(12) Å), both of which have their displacements in [00 $\bar{1}$]_c directions, as well as interactions with the K⁺. The elongation of the O3 oxygen site along the *c*-axis is therefore due to the different local oxygen environments generated by being surrounded by different amounts of Bi³⁺ and K⁺ and correlations between the different displacements of the Bi[011] and the B-site. The Bi[100] site would have little interaction with this oxygen, leading to the compression along the *a*-axis.

The differences between KBMN-KBT and PMN-PT at the MPB become quite apparent when considering Fig. 4e and g, where the displacements from the polyhedral centroids in PMN-PT are not as large. The Pb²⁺ in PMN-PT has a smaller displacement of 0.140 Å off the centroid whereas there are displacements of 0.186(9), 0.441(7), and 0.640(16) Å for K⁺, Bi[011], and Bi[100] respectively. Likewise, the B-site in PMN-PT shows a displacement of 0.064 Å, whereas there is a 0.10128(10) Å displacement in KBMN-KBT. While these differences are stark, there are some interesting similarities, such as the displacement directions. In PMN-PT, the Pb²⁺ and B-site displace in nearly perpendicular directions. The Pb²⁺ has predominantly [001]_c type displacements and the B-site has predominantly [100]_c displacements. The A- and B-site displacements behave the opposite way in $x = 0.88$ of (1-x) KBMN-xKBT. The B-site is displaced in the [00 $\bar{1}$]_c direction and the A-site vector sum is almost entirely in the [100]_c direction. Having A- and B-sites displaced in different directions would indicate that the correlation of displacements is likely incoherent, favoring polar nanoregions over ferroelectric domains.

2.4. Ferroelectric properties

With an understanding of the composition, $x = 0.88$, and the

structure at the MPB established, the evolution of physical properties across the MPB was investigated to isolate the origin of the improved properties. Bipolar polarization versus electric field ($P(E)$) measurements for $x = 0.84, 0.88, \text{ and } 0.94$ at an applied field of 80 kV cm⁻¹ can be seen in Fig. 5a and at various applied fields in Figs. S11–13.

The observed polarization saturation (P_s) is 4.28, 5.01, and 5.85 μC cm⁻²; the remnant polarization (P_r) is 1.15, 1.69, and 2.05 μC cm⁻²; and coercive field (E_c) 35, 39, and 42 kV cm⁻¹ for $x = 0.84, 0.88, \text{ and } 0.94$ respectively. These values are markedly different from (1-y)PMN-yPT where P_s increases to 33, 34, and 40 μC cm⁻²; the P_r decreased to 27, 27, and 21 mC cm⁻²; and E_c increased to 2.8, 3.6, and 8.5 kV cm⁻² for $y = 0.25, 0.32, \text{ and } 0.40$, respectively [34]. The small polarization seen in KBMN-KBT cannot be accounted for by just the reduction in s² cation concentration (50 % Bi³⁺ versus 100 Pb²⁺). For example, 0.945 (Na_{1/2}Bi_{1/2})TiO₃-0.055BaTiO₃ has $P_s = 33.5 \mu\text{C cm}^{-2}$ and $P_r = 29.5 \mu\text{C cm}^{-2}$ illustrating that large polarizations can be accessible with similar compositions [35].

The likely origin of the low polarization is the large Bi[100] displacements and difficulty reorienting this displacement due to strong Bi-O bonds. The strong bonds could likely rearrange with larger applied fields or increased temperature. The strong bonding of the Bi[100] and Bi[011] are also responsible for both the large coercive field and high T_m , which present practical advantages over PMN-PT in thin film and high temperature applications respectively. The strong bonding with the oxygen framework differentiates this system from (Na_{1/2}Bi_{1/2})TiO₃ based systems which have lower coercive fields, likely due to octahedral rotations distributing the bonds over more oxygens [36].

The P_s , P_r , and E_c values in KBMN-KBT change linearly, which is consistent with previous results and the understanding that these materials become more ferroelectric with increasing Ti⁴⁺ on the B-site [10]. From $x = 0.84$ to 0.94 these data show that P_s has increased by 1.57 μC cm⁻² to a value that is only 0.04 μC cm⁻² less than our previously measured values for $x = 1$ [10]. Similarly, E_c has increased by 7 kV cm⁻¹ and is 2 kV cm⁻¹ less than for $x = 1$. However, despite $x = 0.94$ having almost reached the P_s and E_c values of $x = 1$, the P_r values for $x = 0.94$ have increased by 0.91 μC cm⁻² but are still 0.89 μC cm⁻² lower than $x = 1$. This illustrates that the domains in the material align with the applied field, but they do not persist when the field is removed, indicative of persisting relaxor character. This is different from PMN-PT where there is a precipitous change from relaxor to ferroelectric properties at the MPB [12,34,37]. This behavior is consistent with the observation of *Pm* and not *P4mm* symmetry at $x = 0.94$ beyond the MPB. In Figs. S11–13 show that the linearity of polarization as the field is increased changes, indicating domain walls are moving with increasing applied field [38,39]. Additionally, the current as a function of electric field ($I(E)$, Figs. S11–13) shows a peak at E_c due to the flipping of domain directions.

2.5. Dielectric properties

To better understand the compositional impact on the physical properties, the temperature dependence of the dielectric permittivity was investigated. Relaxors are defined by their dielectric properties, which are also intrinsically linked to d_{33}^* [8]. The real (ϵ') and imaginary (ϵ'') components of the dielectric permittivity, the dielectric loss tangent ($\tan(\delta)$), and Curie-Weiss fitting of ϵ' data can be seen in Figs. S14–24 and dielectric constants are tabulated in Table S12. Data at 1 MHz for $x = 0.25, 0.50, 0.84, 0.88, 0.94, \text{ and } 0.98$ from room temperature to 900 K can be seen in Fig. 5b.

These data illustrate that the peak in the permittivity (T_m) increases with increasing Ti⁴⁺ content (Fig. S25). This increase in T_m is indicative of increasing correlation strength between cation displacements, consistent with increasing ferroelectric character. The value of ϵ' at T_m increases from 1082 at $x = 0.5$ up to 2685 for $x = 0.98$. However, despite this change, the room temperature ϵ' values do not change dramatically, ranging from 454 to 677 within the ferroelectric region of the phase

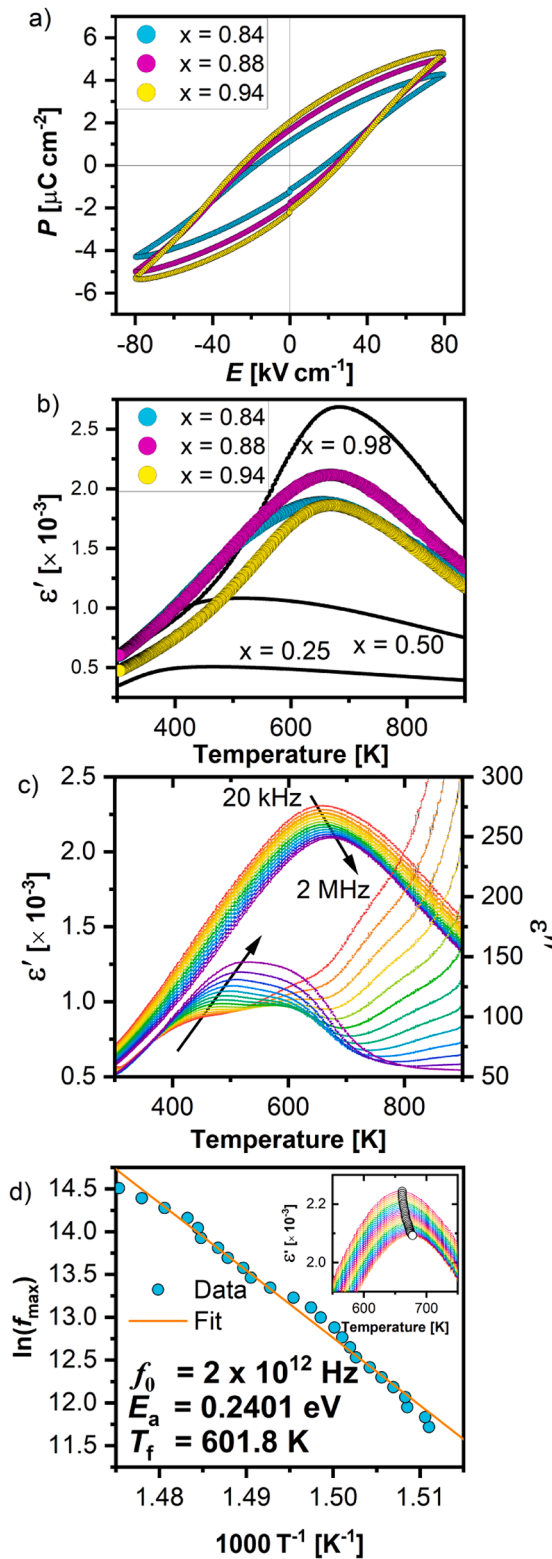


Fig. 5. Physical properties of $(1-x)$ KBMN- x KBT. (a) Polarization as a function of electric field ($P(E)$) loops at a maximum field of 80 kV cm^{-1} for $x = 0.84$, 0.88 , and 0.94 showing ferroelectric character. (b) Dielectric permittivity (ϵ') as a function of temperature at 1 MHz for $x = 0.25$, 0.50 , 0.84 , 0.88 , 0.94 , and 0.98 showing the increase in permittivity and T_m as a function of composition. (c) Dielectric permittivity (ϵ' and ϵ'') as a function of temperature for $x = 0.88$ for frequencies from 20 kHz to 2 MHz and (d) Vogel-Fulcher analysis of the frequency dependence of the permittivity for $x = 0.88$. Inset shows the peak in ϵ' for all measured frequencies from 20 kHz to 2 MHz with their maxima labeled.

diagram ($x \geq 0.7$). T_m increases almost linearly with increasing Ti^{4+} content in the ϵ' , ϵ'' , and $\tan(\delta)$ data, Fig. S25. Dielectric data were analyzed using Curie-Weiss analysis to extract a Weiss constant (θ_W) and Burns temperature (T_B). Positive values of θ_W are seen through the range and indicate ferroelectric interactions, increasing rapidly at the Pm to $P4mm$ phase boundary between $x = 0.98$ and 1 . The increasing T_B values follow the increasing T_m values closely. The T_B gives an estimate of when polar nanoregions dissipate above T_m [8,9,40]. Analysis of KBT above T_m has revealed disordered Bi^{3+} displacements after the material becomes cubic [26]. The observation of room temperature disordered displacements in $x = 0.88$ in combination with the consistent increase in T_B illustrates that a similar effect is happening in this region of the KBMN-KBT phase diagram. All values for T_m , θ_W , and T_B as a function of composition can be seen in Fig. S25 and Table S13.

The variable temperature ϵ' and ϵ'' data for $x = 0.88$ for frequencies from 20 kHz to 2 MHz can be seen in Fig. 5c. A broad frequency dependent peak can be seen in the ϵ' between 600 and 700 K , which is the hallmark of a relaxor. This feature is also present in the ϵ'' , but it is broader. At 1 MHz the value for T_m was determined to be 669 K . The frequency dependence of T_m was analyzed using Vogel-Fulcher fitting to extract the freezing temperature (T_f) and the activation energy (E_a) of polar nanoregions, and the fit can be seen in Fig. 5d. The T_f was determined to be 602 K , which is close to the T_m of 669 K and T_m in PZT (653 K). The 67 K difference between T_f and T_m is much smaller than the 220 K difference seen in KBMN, indicating that this gap is closing with increasing Ti^{4+} content and the relaxor character is decreasing. The E_a was determined to be 240.1 meV , much larger than the 33.0 or 78.6 meV for KBMN or PMN, respectively. This result is consistent with having a much higher T_f and T_m than those materials. The extracted E_a is similar to other relaxors such as $\text{BaTiO}_3\text{-Bi}(\text{Mg}_{1/2}\text{Ti}_{1/2})\text{O}_3$ ($E_a = 219.1 \text{ meV}$) or $\text{BaTiO}_3\text{-BiScO}_3$, ($E_a = 260 \text{ meV}$).

2.6. Piezoresponse force microscopy

The homogenous room temperature ϵ' and the linearly increasing P_s should result in a linearly increasing intrinsic piezoelectric response. However, the piezoelectric response is also impacted by extrinsic factors such as changes to the polar nanoregions and domains. To better understand the origin of the large piezoelectric response at the MPB, piezoresponse force microscopy (PFM) was employed to study the domain structure. The amplitude of the piezoresponse in the lateral direction for $x = 0.84$, 0.88 , and 0.94 can be seen in Fig. 6.

Polar domains represent regions of uniformly orientated polarity and piezoresponse. The large amplitudes (white) represent domains with increased piezoresponse, and the small amplitudes (black) represent regions with decreased piezoresponse. Domain walls are the boundaries between uniform polar regions. An irregular domain structure with curved domain walls is seen in all three samples. Ferroelectrics with tetragonal ($P4mm$) symmetry have 90° or 180° domain walls and 71° or 109.5° domain walls are seen in materials with rhombohedral ($R3m$) symmetry [41,42]. However, many ferroelectrics show deviations from an ideal domain structure, such as $0.6\text{PZT-}0.4\text{Pb}(\text{Fe}_{1/2}\text{Ta}_{1/2})\text{O}_3$ or $\text{Bi}_6(\text{Ti,Fe,Mn})_5\text{O}_{18}$ [42,43]. Irregular domains like those seen in KBMN-KBT have been seen in other relaxors, such as PMN-PT, which transition from irregular to 90° through its MPB [37,44].

Another feature of the domain structure is that the polar domains are nano-sized. The largest domains observed are in $x = 0.94$ (Fig. 6c) at about $1 \mu\text{m}$ in length, but less than $1 \mu\text{m}^2$. Furthermore, the size of domains increases with increasing Ti^{4+} concentration, with average domain sizes of $0.0278 \mu\text{m}^2$ (standard deviation (SD) = $0.0543 \mu\text{m}^2$), $0.0595 \mu\text{m}^2$ (SD = $0.165 \mu\text{m}^2$) and $0.0798 \mu\text{m}^2$ (SD = $0.280 \mu\text{m}^2$) for $x = 0.84$, 0.88 and 0.94 , respectively. A similar variation in size through the MPB in PMN-PT, though PMN-PT has larger domains some which exceed $1 \mu\text{m}$ [44]. This increase in domain size correlates with the trend in ferroelectric properties observed in Fig. 5a. Though $x = 0.94$ has the largest domains, its domain structure is still irregular, with only a few

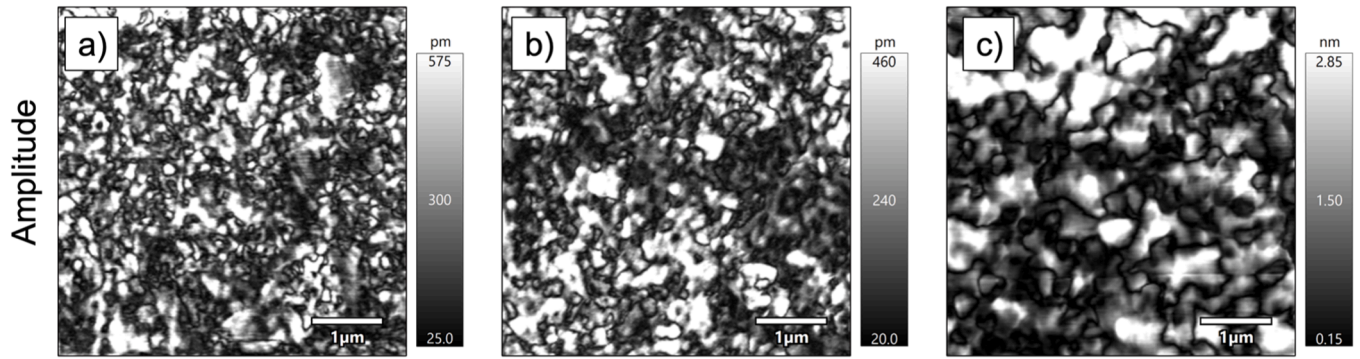


Fig. 6. Piezoresponse force microscopy images for (a) $x = 0.84$, (b) 0.88 , and (c) 0.94 of $(1-x)\text{KBMN}-x\text{KBT}$ showing the lateral piezoresponse amplitudes over a $5 \times 5 \mu\text{m}$ region of a polished ceramic.

regions showing 180° interactions and even fewer with 90° interactions. Despite the transition from smaller to larger domains and the emergence of some regularity to the domain structure there is not a precipitous change which could explain the large increase in d_{33}^* seen for $x = 0.88$. The small, irregular domains are a function of the monoclinic symmetry, which will have twelve domain states as opposed to the six in tetragonal and eight in rhombohedral, and the tendency to form polar nanoregions. Topographies, amplitudes, and phase data in both longitudinal and lateral directions can be seen in Figs. S26–28.

In addition to domain imaging, the electromechanical switching properties can be probed locally by switching spectroscopy PFM (SS-PFM). The phase and amplitude as a function of applied electric field can be seen in Fig. S29. These local polarization switching response data further confirms ferroelectric and piezoelectric properties and the transition from relaxor to ferroelectric character with increasing Ti^{4+} content. The increasing E_c field is observable in the phase component of the SS-PFM data (Fig. S29a–c). The phase of domains switches 180° for all three samples, but the coercive voltage (hysteresis loop width) increases to values of 8.7 , 16.3 , and 20.1 V for $x = 0.84$, 0.88 and 0.94 , respectively. The displacement amplitude as a function of electric field for $x = 0.84$ (Fig. S29d) shows a low and linear response to the applied field, akin to the “sprout” shaped $S(E)$ loops common in relaxor materials. Furthermore, there is only a small negative component (37 pm) arising from ferroelectric domain switching. At $x = 0.88$ (Fig. S29e) the shape of the loop changes to a more “butterfly” shape, indicating ferroelectric character, with a larger negative strain component (81 pm). This negative strain increases even further (102 pm) in loops for $x = 0.94$, Fig. S29f.

While the crossover from relaxor to ferroelectric at the MPB is known in PMN-PT, the details of this crossover in KBMN-KBT are different. The PFM amplitudes as a function of field show that this crossover is seen over a narrow compositional range ($x = 0.84$ – 0.88) like PMN-PT. However, the imaging of the domains, the frequency dependence in the dielectric data, and the change in symmetry with composition shows the persistence of relaxor features into the region where ferroelectric properties are observed, which is a distinction from PMN-PT.

3. Discussion

Looking at these new data together makes identification and understanding the mechanism at the MPB quite clear. The piezoelectric coefficient, both d_{33} or d_{33}^* , is intrinsically dependent on three factors: the dielectric permittivity (ϵ'), the polarization of the material (P), and the electrostriction of the material (Q):

$$d = 2Q\epsilon P$$

The measured permittivity and polarization of materials show a linear trend with composition through the MPB ($x = 0.88$, Fig. 7a). Furthermore, we investigated extrinsic factors contributing to the d_{33}^* ,

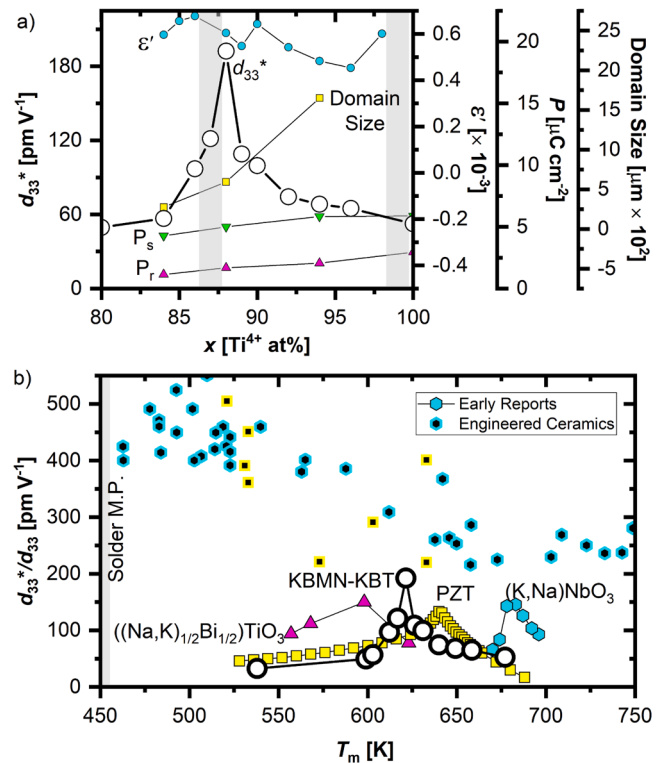


Fig. 7. (a) Compositional dependence of the d_{33}^* (white circles), room temperature ϵ' (cyan circles), the polarization (P_s is green triangles pointing down and P_r is magenta triangles pointing up), and the domain size (yellow squares) determined from PFM measurements. These linear trends of μ' , P_s , and P_r while the d_{33}^* is non-linear vs increasing Ti^{4+} content reveals that the change in symmetry is entirely responsible for the increase in d_{33}^* . (b) The room temperature d_{33}^* or d_{33} as a function of T_m for KBMN-KBT and early reports of $((\text{Na}, \text{K})_{1/2}\text{Bi}_{1/2})\text{TiO}_3$ (magenta triangles), PZT (yellow squares), and $(\text{K}, \text{Na})\text{NbO}_3$ (cyan hexagons). The melting point of solder (~ 450 K) has been highlighted to show that these materials can be assembled as devices. Values for engineered PZT and KNN ceramics have been added for context [50,51].

the domain structure. The observed change with composition showed an expected increase in domain size. The domain structure of all samples unexpectedly showed polar nanoregion type domains, with tetragonal-type domain wall interactions (90° and 180° interactions) forming only at $x = 0.94$. These consistent changes in physical parameters traversing a large change in the d_{33}^* values (Fig. 7a) preclude an entirely intrinsic driving force for the high d_{33}^* . Likewise, no precipitous change in the extrinsic factors can entirely explain the piezoelectric properties. This allows us to conclude that the increase in d_{33}^* is primarily

associated with a change in symmetry and the corresponding flattened free energy profile allowing a polarization rotation [45].

Comparing KBMN-KBT to other piezoelectric materials (Fig. 7b) shows the promise of this new system. At $x = 0.88$ the high field piezoelectric response is 192 pm V^{-1} , which is higher than the first reports of PZT ($d_{33} = 133 \text{ pm V}^{-1}$) [5,46]. Furthermore, early reports on $(\text{Na}_{1-x}\text{K}_x)_{1/2}\text{Bi}_{1/2}\text{TiO}_3$ (NBT-KBT) and $(\text{K}_{1-x}\text{Na}_x)\text{NbO}_3$ (KNN) show lower d_{33} values of 150 and 146 pm V^{-1} respectively [47–49]. The piezoelectric response at room temperature is impacted by the ferroelectric to paraelectric phase transition (T_C) of a material, with high- T_C materials commonly showing a low room temperature d_{33} . Many of these materials have complex phase transitions where $T_C \neq T_m$. Therefore, T_m is generally the best approximation of T_C without extensive further study. Furthermore, we report the high field d_{33} (d_{33}^*) which can be diverge from the low field d_{33} . While there can be divergence between these figures of merit, d_{33}^* is a good estimate of the piezoelectric properties. The d_{33}^* and d_{33} values as a function of T_m for KBMN-KBT along with PZT, NBT-KBT, and KNN can be seen in Fig. 7b. The T_m of KBMN-KBT is in proximity to these other important piezoelectric materials, but demonstrates a larger response than early, unoptimized reports. Importantly, all these materials (KBMN-KBT, PZT, NBT-KBT, and KNN) have T_m values higher than the melting point of the solder used to assemble electronic components, an advantage over PMN-PT when considering device applications. The potential operating temperature and complexities of T_C , T_m , d_{33} , and d_{33}^* illustrate the need for further understanding of this new system due to its fundamental value in understanding Pb-free piezoelectric materials and its potential for practical use.

Another advantage of KBMN-KBT is its low dielectric permittivity at room temperature, $\epsilon' = 604$, while maintaining a large d_{33}^* . Despite a low permittivity's negative impact on d_{33}^* , it is important for thin film applications where the thin piezoelectrics will become capacitors, which will negatively impact adjacent components. The low permittivity in KBMN-KBT is due to the large Bi^{3+} displacements suppressing atomic polarization contributions, and is much lower compared to NBT-KBT, and KNN which show $\epsilon' = 825$ and 721, respectively [47–49]. Despite showing a larger d_{33}^* than early reports of other materials, optimization of ceramic processing, poling conditions, and dopants has since generated great improvements in PZT, NBT-KBT, KNN and BT-BF. The d_{33} of PZT can be increased to as high as 640 pm V^{-1} and KNN has been reported as high as 570 pm V^{-1} [5,52]. These improvements over early reports show that with extensive ceramic processing and carefully selected dopants the piezoelectric properties of KBMN-KBT could be increased further. Another avenue for improvement would be identifying single crystal growth parameters, which can more than double the piezoelectric properties of PMN-PT.

4. Conclusions

We have compositionally explored the $(1-x)\text{KBMN}-x\text{KBT}$ solid solution which demonstrates enhanced performance at the composition $x = 0.88$ and an MPB between $x = 0.86$ and 0.88. Our detailed structural analysis of $x = 0.88$ yields average and local structural insights, allowing us to understand the impact of the structure on the physical response. The average structure has Pm (M_C) symmetry with a small deviations from cubic, like the best performing $(1-y)\text{PMN}-y\text{PT}$ composition, $y = 0.32$. Displacements of the K^+ and Bi^{3+} cations persist but re-organize from the KBMN endmember ($x = 0$), despite multiple changes in symmetry. The large displacements are driven by the strong bonding between Bi^{3+} and oxygen and dictates the physical response. The majority of the Bi^{3+} (74.4 %, $\text{Bi}[011]$) forms three short bonds akin to the rhombohedral-type bonding environment found in the vast majority of Bi^{3+} ferroelectrics. Despite this bonding environment being reminiscent of a rhombohedral symmetry, the displacement from the centroid is $[011]_c$ in nature, different from a rhombohedral $[111]_c$ type displacement and an uncommon displacement direction for Bi-based materials.

The existence of the $\text{Bi}[011]$ site between endmembers which prefer $[001]_c \text{Bi}^{3+}$ displacements indicates that the s^2 electronic configuration of Bi^{3+} creates this local environment, thereby driving both the average structure and bulk properties. This environment appears key to generating the MPB and improved properties seen KBMN-KBT. The dielectric and ferroelectric properties as well as the domain structure evolve linearly across the MPB, despite the increased piezoelectric response. This allows us to isolate intrinsic and extrinsic factors to the piezoelectric response and confidently assign the mechanism of improved piezoelectric response to a change in symmetry, i.e. a polarization rotation. Our multiple length-scale perspective describing local (MEM and bond lengths), short-range (PFM), and average (Rietveld) structural information provides a balanced description of the structure and mechanism, allowing us to isolate the origin of the properties to the local chemical configuration to Bi^{3+} . The composition and average structural progression through the solid solution affords a strong analogy to PMN-PT, yet the properties, short-range order, and local chemistry are distinct. This level of analysis reveals KBMN-KBT to be a competitive Pb-free piezoelectric and yields insights into strategies for optimization.

5. Methods

Samples of $(1-x)(\text{K}_{1/2}\text{Bi}_{1/2})(\text{Mg}_{1/3}\text{Nb}_{2/3})\text{O}_3-x(\text{K}_{1/2}\text{Bi}_{1/2})\text{TiO}_3$ ($(1-x)\text{KBMN}-x\text{KBT}$) were synthesized in the range $x = 0.84$ and 0.98, in $x = 0.02$ steps using solid-state synthesis, as described previously [10]. A MgNb_2O_6 columbite precursor was used to suppress the formation of $(\text{Bi}, \text{Mg})_2(\text{Mg}, \text{Nb})_2\text{O}_7$ pyrochlore impurities. Stoichiometric amounts of $(\text{MgCO}_3)_4\text{Mg}(\text{OH})_2 \cdot 5\text{H}_2\text{O}$ (99.99 %, Sigma) and Nb_2O_5 (99.9985 %, Alfa Aesar) were ground in an agate pestle and mortar and fired in an alumina crucible at 1723 K for 3 h using a ramp rate of 5 K/min on heating and cooling to produce a phase pure product. This product was then used in stoichiometric amounts with Bi_2O_3 (99.999 %, Alfa Aesar), K_2CO_3 (99.997 %, Alfa Aesar), and TiO_2 (99.995 %, Alfa Aesar) and mixed in an agate pestle and mortar with a target batch size of 20 g. The mixed reagents were then ball milled in a Fritsch Pullverisette rotary mill in zirconia pots with seven 10 mm zirconia balls as a milling media in 10 mL of ethanol. Milling conditions were 350 RPM for 15 min, resting for 10 min, then repeating this cycle in the opposite direction for 20 cycles. After milling samples were dried and fired in air at 1123 K for 3 h in an alumina crucible, reground, pressed into 10 mm cylindrical pellets, covered in sacrificial powder of the same composition, and fired in covered alumina crucibles at 1273 K for 12 h twice, with grinding in an agate pestle and mortar done between each heating step. This process achieved pure phase powdered samples.

The composition of the $x = 0.88$ sample was confirmed by energy-dispersive X-ray spectroscopy (EDX) data collected using a JEOL2100+ operating at 200 kV equipped with an Oxford Instruments X-Max 65T silicon drift detector. Samples were dispersed on carbon coated copper TEM grids and were inserted using a single tilt holder. Data acquisition and analysis were performed using the Aztec software. Correction factors were determined measuring proper standards for each chemical element. Small, isolated particles were picked for EDX analysis to avoid collecting data from agglomerates and 10 particles were measured per composition to determine homogeneity.

Synchrotron XRD data were collected in Debye-Scherrer (transmission) mode at room temperature on the powder diffraction end-station at the BL04-MSPD beamline at the ALBA synchrotron light source (Barcelona, Spain) [53]. An incident X-ray wavelength of 0.4131 Å was used. Samples were loaded into glass capillaries, spun during data collection to improve particle statistics, and measured using the MYTHEN detector. The measurement time for each diffraction pattern was 1 min. The same samples were sent to Oak Ridge National Lab to perform neutron powder diffraction (NPD) experiments at room temperature at the POWGEN instrument at the Spallation Neutron Source. Approximately 8 g of sample were placed into 6 mm diameter vanadium cans and loaded in the POWGEN automatic changer [54,55]. The

measurement time was approximately 2 h. A central wavelength of 0.8 Å was used, covering a d -spacing of 0.16–7.87 Å.

Data were analyzed by the Pawley and Rietveld methods using Topas6 Academic [56]. Pawley fits of XRD data were performed from 3 to 23.5° using a Chebyshev polynomial as a background function. The background function needed 18 terms to fit the significant undulation of the background understood to come from diffuse scattering. Peak profiles were fit using the Stephens model. During Rietveld refinement of $x = 0.88$, XRD data from 2.5 to 42° were fit and the background was fit manually using a combination of a linear interpolation of 36 points and three pseudo-Voigt terms. The background of NPD data was fit with a 12 term Chebyshev polynomial and profiles for both data sets were fit with the Stephens model. For atoms which occupy the same site (e.g. Mg²⁺, Nb⁵⁺, Ti⁴⁺ on the B-site of the perovskite structure) atomic positions and atomic displacement parameters were constrained to be equal. All occupancies were constrained to match the nominal stoichiometry of the samples as we previously reported this synthesis method to produce stoichiometric compounds using multiple analytical methods [10]. Atomic displacement parameters were fit isotropically (B_{iso}) for all cations, and anisotropically for oxygen ions due to a large B_{iso} value found for the O3 position. All atomic positions, lattice parameters, profile parameters, zero errors, occupancies, and atomic displacement parameters were refined simultaneously to yield the reported refinements. Maximum entropy method calculations were performed using BayMEM with Jana200 generating the input [57,58]. Electron densities were visualized using VESTA [59]. A crystallographic information format (CIF) file for $x = 0.88$ has been submitted with this publication, CSD 2216362.

Pure phase powders were sintered using spark plasma sintering (SPS) in a Thermal Technology LLC DCS10 furnace. Approximately 0.75 g of material was loaded into a 10 mm diameter graphite die lined with graphite foil. The chamber was evacuated to $<5 \times 10^{-2}$ mbar and 60 MPa of pressure was applied uniaxially to the sample before backfilling with He. Samples were heated to 1023 K at 100 K/min and then up to 1223 K at 200 K/min for a duration of 1 min before cooling in the same manner. Temperatures were monitored using an optical pyrometer centered on a bore hole in the side of the die. After sintering, samples were removed from dies and the graphite foil from surfaces. Samples were heated in a tube furnace under flowing O₂ to 1123 K for 12 h using a heating and cooling rate of 5 K/min to remove any remaining graphite and ensure the sample is fully oxidized, thereby suppressing conductivity, and relieving stress at the grain boundaries. After this process, the density was assessed using the Archimedes method. Densities were 95 % or greater for all samples.

Dense samples were polished using a Struers automatic polishing machine to achieve the optimal thickness and surface roughness. Samples for dielectric analysis were polished to a thickness of 1.0 – 0.5 mm with #800 and #1200 SiC foils. Samples were electroded with high temperature gold paste (Koartan 4129) which was fired on at 973 K for 30 min with a ramp rate of 5 K/min on heating and cooling. An Agilent 4980 LCR meter with a home-built sample holder and LABVIEW controller was used to collect real component (ϵ') of the dielectric permittivity and the dielectric loss tangent ($\tan(\delta)$). These values were used to calculate the imaginary component (ϵ'') of the dielectric permittivity. Data were collected from 20 Hz to 2 MHz and at temperatures from room temperature to 923 K. Data on cooling and data was analyzed as thermally activated defects will have migrated, mitigating their contribution to the data. The Weiss constant (q_w) was determined by fitting the inverse of the ϵ' data at 1 MHz using Curie-Weiss Law and the Burns temperature (T_B) was extracted from where the data deviated from the Curie-Weiss fit.

Samples for ferroelectric and piezoelectric measurements were polished to a thickness of 0.5 – 0.2 ± 0.01 mm with #800, #1200, and #4000 SiC foils until they had a mirror finish. Samples were then sputtered with gold electrodes for measurement. Polarization ($P(E)$), strain ($S(E)$), and current ($I(E)$) as a function of electric field were

measured using an aixPES instrument (aixACCT GmbH Germany) at room temperature. Data were measured at 1 Hz to ensure sufficient time for domains to react to the applied field. All ferroelectric and piezoelectric constants were taken from measurements at 80 kV cm⁻¹.

Local electromechanical responses of the films were measured by PFM (piezoresponse force microscopy) using an Asylum Research MFP-3D™ AFM in contact mode equipped with a HVA220 Amplifier for PFM and a cantilever scan angle of 90°. Olympus AC240™ Electrilevers, Ti/Pt coated silicon probes (Al reflex coated, 15 nm tip radius, 70 kHz resonant frequency), were used for PFM and topography imaging. The Inverse Optical Lever Sensitivity of the cantilevers was calibrated according to the MFP-3D Procedural Operation ‘Manualette’. The Dual AC (alternating current) Resonance Tracking PFM (DART-PFM) mode was used to boost both the vertical and lateral piezo signals. In this mode, the PFM signal is measured at the tip-sample contact resonance frequency, with higher signal-to-noise ratio compared with other frequencies. Topographical cross-talk is reduced using an amplitude feedback loop which tracks the contact resonance frequency so that drive frequencies are adjusted accordingly as the probe scans over the changing sample topography. Application of an AC bias to a conductive tip during contact mode imaging ($V_{tip} = V_{AC} \cos(\omega t)$) results in surface displacement (d) and deflection of cantilever due to the converse piezoelectric effect, with both normal and in-plane components. The read step was performed with probing signals of 3.0 V_{AC}. The angular torsion of the cantilever as it oscillates was monitored in lateral PFM measurements, which were conducted in a similar manner to the vertical PFM measurements except the ‘InFast’ option was programmed to ‘Lateral’ as opposed to ‘AC Deflection’ and the drive frequencies were operated near contact resonance for lateral (740 to 800 kHz) and vertical (280 320 kHz) modes respectively. Vertical hysteresis loop measurements were obtained by switching spectroscopy PFM (SS-PFM) after the removal of an applied pulsed DC bias (“field off state”) using a triangular step waveform (comprised of pulse DC bias voltage (35 V) and an AC signal (3.0 V)). The waveform was cycled twice at a frequency of 0.3 Hz with 68 AC steps per waveform. Note that the “field on” loops are not presented here, since electrostrictive effects and electrostatic interactions between the cantilever and the back electrode can complicate the interpretation of the hysteresis loops obtained.

Declaration of Competing Interest

The authors declare that they have no known competing financial interests or personal relationships that could have appeared to influence the work reported in this paper.

Acknowledgments

We thank the EPSRC (EP/R011753, EP/R010293, and EP/N004884) for funding this research. We would like to thank Alba Synchrotron Light Source (MSPD) for supporting this research. A portion of this research used resources at the Spallation Neutron Source, a DOE Office of Science User Facility operated by the Oak Ridge National Laboratory (IPTS-25965.1 for POWGEN experiment) for supporting this research through their user programmes. This research was partially funded by ASCENT+ Access to European Infrastructure for Nanoelectronics (EU Horizon 2020 Programme Grant No 871130) and the Royal Irish Academy / Royal Society International Exchange Cost-Share Programme 2019. We acknowledge the ICSF Faraday Challenge Project “All-Solid-State Lithium Anode Battery” [Grant No. FIRG026] for funding the studentship of A.M. L.K. would like to thank her support from the Royal Society and Science Foundation Ireland University Fellowship URF\R\201008. We thank the Leverhulme Trust through the Leverhulme Research Centre for Functional Materials Design (RC-2015-036).

Supplementary materials

Supplementary material associated with this article can be found, in the online version, at [doi:10.1016/j.actamat.2023.119594](https://doi.org/10.1016/j.actamat.2023.119594).

References

- [1] A.M. Manjón-Sanz, M.R. Dolgos, Applications of Piezoelectrics: Old and New, *Chemistry of Materials* 30 (2018) 8718–8726, <https://doi.org/10.1021/acs.chemmater.8b03296>.
- [2] S. Mohith, A.R. Upadhyaya, K.P. Navin, S.M. Kulkarni, M. Rao, Recent trends in piezoelectric actuators for precision motion and their applications: a review, *Smart Mater Struct* 30 (2021), <https://doi.org/10.1088/1361-665X/abc6b9>.
- [3] T.B. Xu, Energy harvesting using piezoelectric materials in aerospace structures, *Structural Health Monitoring in Aerospace Structures*. 10.1016/B978-0-08-100148-6.00007-X.
- [4] D. Demartin Maeder, D. Damjanovic, N. Setter, Lead free piezoelectric materials, *J Electroceram* 13 (2004) 385–392, <https://doi.org/10.1007/s10832-004-5130-y>.
- [5] B. Jaffe, W.R. Cook, H.L. Jaffe. *Piezoelectric Ceramics*, Academic Press, New York, 1971, <https://doi.org/10.1016/B978-0-12-379550-2.X5001-7>.
- [6] F. Li, M.J. Cabral, B. Xu, Z. Cheng, E.C. Dickey, J.M. LeBeau, J. Wang, J. Luo, S. Taylor, W. Hackenberger, L. Bellaiche, Z. Xu, L.-Q. Chen, T.R. Shrout, S. Zhang, Giant piezoelectricity of Sm-doped $\text{PbMg}_{1/3}\text{Nb}_{2/3}\text{O}_3$ - PbTiO_3 single crystals, *Science* 364 (2019) 264–268, <https://doi.org/10.1126/science.aaw2781>.
- [7] J. Kelly, M. Leonard, C. Tantigate, A. Safari, Effect of composition on the electromechanical properties of (1-x)Pb($\text{Mg}_{1/3}\text{Nb}_{2/3}$) O_3 -xPbTiO₃ ceramics, *Journal of the American Ceramic Society* 80 (1997) 957–964, <https://doi.org/10.1111/j.1151-2916.1997.tb02927.x>.
- [8] A.A. Bokov, Z.G. Ye, Recent progress in relaxor ferroelectrics with perovskite structure, *J Mater Sci* 41 (2006) 31–52, <https://doi.org/10.1007/s10853-005-5915-7>.
- [9] A.A. Bokov, Z. Ye, Dielectric Relaxation in Relaxor Ferroelectrics, *J Adv Dielectr*. 02 (2012) 1241010. 10.1142/s2010135x1241010x.
- [10] T.W. Surta, T.A. Whittle, M.A. Wright, H. Niu, J. Gamon, Q.D. Gibson, L. M. Daniels, W.J. Thomas, M. Zanella, P.M. Shepley, Y. Li, A. Goetze-Barral, A. J. Bell, J. Alaria, J.B. Claridge, M.J. Rosseinsky, One Site, Two Cations, Three Environments: s² and s⁰ Electronic Configurations Generate Pb-Free Relaxor Behavior in a Perovskite Oxide, *J Am Chem Soc* 143 (2021) 1386–1398, <https://doi.org/10.1021/jacs.0c10572>.
- [11] D. Phelan, E.E. Rodriguez, J. Gao, Y. Bing, Z.G. Ye, Q. Huang, J. Wen, G. Xu, C. Stock, M. Matsuura, P.M. Gehring, Phase diagram of the relaxor ferroelectric (1-x)Pb($\text{Mg}_{1/3}\text{Nb}_{2/3}$) O_3 -xPbTiO₃ revisited: A neutron powder diffraction study of the relaxor skin effect, *Phase Transitions* 88 (2015) 283–305, <https://doi.org/10.1080/01411594.2014.989226>.
- [12] M.J. Krogstad, P.M. Gehring, S. Rosenkranz, R. Osborn, F. Ye, Y. Liu, J.P.C. Ruff, W. Chen, J.M. Wozniak, H. Luo, O. Chmaissem, Z.G. Ye, D. Phelan, The relation of local order to materials properties in relaxor ferroelectrics, *Nat Mater* 17 (2018) 718–724, <https://doi.org/10.1038/s41563-018-0112-7>.
- [13] A.K. Singh, D. Pandey, O. Zaharko, Powder neutron diffraction study of phase transitions in and a phase diagram of (1-x)[Pb($\text{Mg}_{1/3}\text{Nb}_{2/3}$) O_3]-xPbTiO₃, *Phys Rev B* 74 (2006) 1–18, <https://doi.org/10.1103/PhysRevB.74.024101>.
- [14] V.A. Isupov, Ferroelectric $\text{Na}_{0.5}\text{Bi}_{0.5}\text{TiO}_3$ and $\text{K}_{0.5}\text{Bi}_{0.5}\text{TiO}_3$ perovskites and their solid solutions, *Ferroelectrics* 315 (2005) 123–147, <https://doi.org/10.1080/001501990910276>.
- [15] Y. Hiruma, K. Marumo, R. Aoyagi, H. Nagata, T. Takenaka, Ferroelectric and piezoelectric properties of ($\text{Bi}_{1/2}\text{K}_{1/2}$)TiO₃ ceramics fabricated by hot-pressing method, *J Electroceram* 21 (2008) 296–299, <https://doi.org/10.1007/s10832-007-9146-y>.
- [16] Y. Hiruma, R. Aoyagi, H. Nagata, T. Takenaka, Ferroelectric and Piezoelectric Properties of ($\text{Bi}_{1/2}\text{K}_{1/2}$)TiO₃ Ceramics, *Jpn J Appl Phys* 44 (2005) 5040–5044, <https://doi.org/10.1143/JJAP.44.5040>.
- [17] B. Noheda, D.E. Cox, G. Shirane, J. Gao, Z.G. Ye, Phase diagram of the ferroelectric relaxor (1-x)Pb($\text{Mg}_{1/3}\text{Nb}_{2/3}$) O_3 -xPbTiO₃, *Phys Rev B* 66 (2002) 1–10, <https://doi.org/10.1103/PhysRevB.66.054104>.
- [18] B. Noheda, Structure and high-piezoelectricity in lead oxide solid solutions, *Curr Opin Solid State Mater Sci* 6 (2002) 27–34, [https://doi.org/10.1016/S1359-0286\(02\)00015-3](https://doi.org/10.1016/S1359-0286(02)00015-3).
- [19] P. Bonneau, P. Garnier, G. Calvarin, E. Husson, J.R. Gavarri, A.W. Hewat, A. Morell, X-ray and neutron diffraction studies of the diffuse phase transition in ceramics, *J Solid State Chem* 91 (1991) 350–361, [https://doi.org/10.1016/0022-4596\(91\)90090-5](https://doi.org/10.1016/0022-4596(91)90090-5).
- [20] T.W. Surta, A. Manjón-Sanz, E. Qian, T.T. Tran, M.R. Dolgos, Low temperature synthesis route and structural characterization of ($\text{Bi}_{0.5}\text{A}_{0.5}$)($\text{Sc}_{0.5}\text{Nb}_{0.5}$) O_3 (A = K⁺ and Na⁺) perovskites, *Inorg Chem Front* 5 (2018) 1033–1044, <https://doi.org/10.1039/C8QI00144H>.
- [21] C. Perrin, N. Menguy, E. Suard, C. Muller, C. Caranoni, A. Stepanov, Neutron diffraction study of the relaxor – ferroelectric phase transition in disordered Pb ($\text{Sc}_{1/2}\text{Nb}_{1/2}$) O_3 , *J. Phys.: Condens. Matter*. 12 (2000) 7523–7539, <https://doi.org/10.1088/0953-8984/12/33/317>.
- [22] A. Manjón-Sanz, T.W. Surta, P. Mandal, A.J. Corkett, H. Niu, E. Nishibori, M. Takata, J.B. Claridge, M.J. Rosseinsky, Complex Structural Disorder in a Polar Orthorhombic Perovskite Observed through the Maximum Entropy Method / Rietveld Technique, *Chemistry of Materials* 34 (2022) 29–32, <https://doi.org/10.1021/acs.chemmater.1c01979>.
- [23] K. Shoto, M. Eisuke, M. Chikako, K. Yoshihiro, T. Nao, T. Hiroshi, M. Sachiko, T. Masaki, W. Satoshi, Electronic Polarization in KNbO₃ Visualized by Synchrotron Radiation Powder Diffraction, *Jpn J Appl Phys* 52 (2013) 09KF04, <https://doi.org/10.7567/JJAP.52.09KF04>.
- [24] R. Haumont, I.A. Kornev, S. Lisenkov, L. Bellaiche, J. Kreisel, B. Dkhil, Phase stability and structural temperature dependence in powdered multiferroic BiFeO₃, *Phys Rev B* 78 (2008) 1–8, <https://doi.org/10.1103/PhysRevB.78.134108>.
- [25] C.A. Bridges, M. Allix, M.R. Suchomel, X. Kuang, I. Sterianou, D.C. Sinclair, M. J. Rosseinsky, A pure bismuth a site polar perovskite synthesized at ambient pressure, *Angewandte Chemie - International Edition* 46 (2007) 8785–8789, <https://doi.org/10.1002/anie.200703146>.
- [26] I. Levin, D.S. Keeble, G. Gibin, H.Y. Playford, M. Eremenko, V. Krayzman, W. J. Laws, I.M. Reaney, Nanoscale Polar Heterogeneities and Branching Bi-Displacement Directions in $\text{K}_{0.5}\text{Bi}_{0.5}\text{TiO}_3$, *Chemistry of Materials* 31 (2019) 2450–2458, <https://doi.org/10.1021/acs.chemmater.8b05187>.
- [27] S. Kim, I. Fujii, S. Ueno, Y. Nakahira, Y. Sato, S. Wada, Piezoelectricity in perovskite-type pseudo-cubic ferroelectrics by partial ordering of off-centered cations, *Commun Mater* 1 (2020) 1–8, <https://doi.org/10.1038/s43246-020-00072-4>.
- [28] A. Singh, C. Moriyoshi, Y. Kuroiwa, D. Pandey, Evidence for local monoclinic structure, in: polarization rotation , and morphotropic phase transitions in (1-x)BiFeO₃-xBaTiO₃ solid solutions: A high-energy synchrotron x-ray powder diffraction study, 2013, pp. 1–12, <https://doi.org/10.1103/PhysRevB.88.024113>, 024113.
- [29] C. Moriyoshi, S. Takeda, Y. Kuroiwa, M. Goto, Off-centering of a Bi ion in cubic phase of ($\text{Na}_{1/2}\text{Bi}_{1/2}$)TiO₃, *Jpn J Appl Phys*. 53 (2014) 09PD02. 10.7567/JJAP.53.09PD02.
- [30] A. Singh, C. Moriyoshi, Y. Kuroiwa, D. Pandey, Visualization of Bi3⁺ off-centering in the average cubic structure of ($\text{Ba}_{0.70}\text{Bi}_{0.30}$)($\text{Ti}_{0.70}\text{Fe}_{0.30}$) O_3 at the electron density level, *Appl Phys Lett* 121907 (2013) 0–4, <https://doi.org/10.1063/1.4822032>.
- [31] S. Kim, H. Nam, I. Fujii, S. Ueno, C. Moriyoshi, Y. Kuroiwa, S. Wada, A-site cation off-centering contribution on ferroelectricity and piezoelectricity in pseudo-cubic perovskite structure of Bi-based lead-free piezoelectrics, *Scr Mater* 205 (2021) 114176, <https://doi.org/10.1016/j.scriptamat.2021.114176>.
- [32] P. Mandal, A. Manjón-Sanz, A.J. Corkett, T.P. Comyn, K. Dawson, T. Stevenson, J. Bennett, L.F. Henrichs, A.J. Bell, E. Nishibori, M. Takata, M. Zanella, M. R. Dolgos, U. Adem, X. Wan, M.J. Pitcher, S. Romani, T.T. Tran, P.S. Halasyamani, J.B. Claridge, M.J. Rosseinsky, Morphotropic phase boundary in the Pb-Free (1-x)BiTi_{3/8}Fe_{2/8}Mg_{3/8}O₃-xCaTiO₃ System: Tetragonal polarization and enhanced electromechanical properties, *Advanced Materials* 27 (2015) 2883–2889, <https://doi.org/10.1002/adma.201405452>.
- [33] M. Dolgos, U. Adem, X. Wan, Z. Xu, A.J. Bell, T.P. Comyn, T. Stevenson, J. Bennett, J.B. Claridge, M.J. Rosseinsky, Chemical control of octahedral tilting and off-axis A cation displacement allows ferroelectric switching in a bismuth-based perovskite, *Chem Sci* 3 (2012) 1426–1435, <https://doi.org/10.1039/c2sc01115h>.
- [34] R. Zuo, T. Granzow, D.C. Lupascu, J. Rödel, PMN-PT ceramics prepared by spark plasma sintering, *Journal of the American Ceramic Society* 90 (2007) 1101–1106, <https://doi.org/10.1111/j.1551-2916.2007.01533.x>.
- [35] R. McQuade, T. Rowe, A. Manjón-Sanz, L. de la Puente, M.R. Dolgos, An investigation into group 13 (Al, Ga, In) substituted ($\text{Na}_{0.5}\text{Bi}_{0.5}$)TiO₃-BaTiO₃ (NBT-BT) lead-free piezoelectrics, *J Alloys Compd* 762 (2018) 378–388, <https://doi.org/10.1016/j.jallcom.2018.04.329>.
- [36] V.R. Mudinepalli, F. Leng, M.P. Reddy, W.C. Lin, B.S. Murty, Structural, dielectric and ferroelectric properties of lead-free $\text{Na}_{0.5}\text{Bi}_{0.5}\text{TiO}_3$ ceramics prepared by spark plasma sintering technique, *Indian Journal of Physics* 90 (2016) 131–138, <https://doi.org/10.1007/s12648-015-0743-3>.
- [37] M. Otonicar, H. Ursic, M. Dragomir, A. Bradesko, G. Esteves, J.L. Jones, A. Bencan, B. Malic, T. Rojac, Multiscale field-induced structure of (1-x)Pb($\text{Mg}_{1/3}\text{Nb}_{2/3}$) O_3 -xPbTiO₃ ceramics from combined techniques, *Acta Mater* 154 (2018) 14–24, <https://doi.org/10.1016/j.actamat.2018.05.028>.
- [38] S. Li, W. Cao, L.E. Cross, The extrinsic nature of nonlinear behavior observed in lead zirconate titanate ferroelectric ceramic, *J Appl Phys* 69 (1991) 7219–7224, <https://doi.org/10.1063/1.347616>.
- [39] M.R. Dolgos, U. Adem, A. Manjón-Sanz, X. Wan, T.P. Comyn, T. Stevenson, J. Bennett, A.J. Bell, T.T. Tran, P.S. Halasyamani, J.B. Claridge, M.J. Rosseinsky, Perovskite B-site compositional control of [110]_p polar displacement coupling in an ambient-pressure-stable bismuth-based ferroelectric, *Angewandte Chemie - International Edition* 51 (2012) 10770–10775, <https://doi.org/10.1002/anie.201203884>.
- [40] J. Toulouse, The Three Characteristic Temperatures of Relaxor Dynamics and Their Meaning, *Ferroelectrics* 369 (2008) 203–213, <https://doi.org/10.1080/08838150802378160>.
- [41] A.J. Bell, P.M. Shepley, Y. Li, Domain wall contributions to piezoelectricity in relaxor-lead titanate single crystals, *Acta Mater* 195 (2020) 292–303, <https://doi.org/10.1016/j.actamat.2020.05.034>.
- [42] D.M. Evans, A. Schilling, A. Kumar, D. Sanchez, N. Ortega, M. Arredondo, R. S. Katiyar, J.M. Gregg, J.F. Scott, Magnetic switching of ferroelectric domains at room temperature in multiferroic PZTFT, *Nat Commun* 4 (2013) 1–7, <https://doi.org/10.1038/ncomms2548>.
- [43] K. Moore, E.N. O'Connell, S.M. Griffin, C. Downing, L. Colfer, M. Schmidt, V. Nicolosi, U. Bangert, L. Keeney, M. Conroy, Charged Domain Wall and Polar Vortex Topologies in a Room-Temperature Magnetoelectric Multiferroic Thin Film, *ACS Appl Mater Interfaces* 14 (2022) 5525–5536, <https://doi.org/10.1021/acsami.1c17383>.

- [44] K.Y. Zhao, W. Zhao, H.R. Zeng, H.Z. Yu, W. Ruan, K.Q. Xu, G.R. Li, Tip-bias-induced domain evolution in PMN-PT transparent ceramics via piezoresponse force microscopy, *Appl Surf Sci* 337 (2015) 125–129, <https://doi.org/10.1016/j.apsusc.2015.02.075>.
- [45] D. Damjanovic, Contributions to the piezoelectric effect in ferroelectric single crystals and ceramics, *Journal of the American Ceramic Society* 88 (2005) 2663–2676, <https://doi.org/10.1111/j.1551-2916.2005.00671.x>.
- [46] H. Jaffe, Piezoelectric Ceramics, *Journal of the American Ceramic Society* 41 (1958) 494–498, <https://doi.org/10.1111/j.1151-2916.1958.tb12903.x>.
- [47] S. Zhao, G. Li, A. Ding, T. Wang, Q. Yin, Ferroelectric and piezoelectric properties of $(\text{Na}, \text{K})_{0.5}\text{Bi}_{0.5}\text{TiO}_3$ lead free ceramics, *J Phys D Appl Phys* 39 (2006) 2277–2281, <https://doi.org/10.1088/0022-3727/39/10/042>.
- [48] B.P. Zhang, J.F. Li, K. Wang, H. Zhang, Compositional dependence of piezoelectric properties in $\text{Na}_x\text{K}_{1-x}\text{NbO}_3$ lead-free ceramics prepared by spark plasma sintering, *Journal of the American Ceramic Society* 89 (2006) 1605–1609, <https://doi.org/10.1111/j.1551-2916.2006.00960.x>.
- [49] Y. Wei, J. Zhu, X. Wang, J. Jia, X. Wang, Dielectric, ferroelectric, and piezoelectric properties of BiFeO_3 - BaTiO_3 ceramics, *Journal of the American Ceramic Society* 96 (2013) 3163–3168, <https://doi.org/10.1111/jace.12475>.
- [50] T.R. Shrout, S.J. Zhang, Lead-free piezoelectric ceramics: Alternatives for PZT? *J Electroceram* 19 (2007) 111–124, <https://doi.org/10.1007/s10832-007-9047-0>.
- [51] H.C. Thong, C. Zhao, Z. Zhou, C.F. Wu, Y.X. Liu, Z.Z. Du, J.F. Li, W. Gong, K. Wang, Technology transfer of lead-free $(\text{K}, \text{Na})\text{NbO}_3$ -based piezoelectric ceramics, *Materials Today* 29 (2019) 37–48, <https://doi.org/10.1016/j.mattod.2019.04.016>.
- [52] D. Damjanovic, N. Klein, J. Li, V. Porokhonsky, What can be expected from lead-free piezoelectric materials? *Functional Materials Letters* 3 (2010) 5–13, <https://doi.org/10.1142/S1793604710000919>.
- [53] F. Fauth, I. Peral, C. Popescu, M. Knapp, The new Material Science Powder Diffraction beamline at ALBA Synchrotron, *Powder Diffr* 28 (2013) 360–370, <https://doi.org/10.1017/S0885715613000900>.
- [54] A. Huq, M. Kirkham, P.F. Peterson, J.P. Hodges, P.S. Whitfield, K. Page, T. Huggle, E.B. Iverson, A. Parizzia, G. Rennichb, POWGEN: Rebuild of a third-generation powder diffractometer at the Spallation Neutron Source, *J Appl Crystallogr.* 52 (2019) 1189–1201. [10.1107/S160057671901121X](https://doi.org/10.1107/S160057671901121X).
- [55] A. Huq, J.P. Hodges, O. Gourdon, L. Heroux, Powgen: A third-generation high-resolution high-throughput powder diffraction instrument at the Spallation Neutron Source, *Zeitschrift Für Kristallographie Proceedings.* 1 (2011) 127–135. [10.1524/9783486991321-024](https://doi.org/10.1524/9783486991321-024).
- [56] A. Coelho, Whole-profile structure solution from powder diffraction data using simulated annealing, *J Appl Crystallogr* 33 (2000) 899–908, <https://doi.org/10.1107/S002188980000248X>.
- [57] S. Van Smaalen, L. Palatinus, M. Schneider, The maximum-entropy method in superspace, *Acta Crystallogr A* 59 (2003) 459–469, <https://doi.org/10.1107/S010876730301434X>.
- [58] V. Petříček, M. Dušek, L. Palatinus, Crystallographic computing system JANA2006: General features, *Zeitschrift Fur Kristallographie* 229 (2014) 345–352, <https://doi.org/10.1515/zkri-2014-1737>.
- [59] K. Momma, F. Izumi, VESTA 3 for three-dimensional visualization of crystal, volumetric and morphology data, *J Appl Crystallogr* 44 (2011) 1272–1276, <https://doi.org/10.1107/S0021889811038970>.